Microtissue geometry and cell-generated forces drive patterning of liver progenitor cell differentiation in 3D

Authors

Ian C. Berg,[a] Erfan Mohagheghian[b], Krista Habing [a], Ning Wang[b], Gregory H. Underhill[a*]

Affiliations

[a]University of Illinois at Urbana-Champaign Department of Bioengineering
1102 Everitt Lab, MC-278
1406 W. Green Street
Urbana, IL 61801, USA

[b]University of Illinois at Urbana-Champaign Department of Mechanical Science and Engineering
Mechanical Engineering Building
1206 W. Green St. MC 244
Urbana, IL, 61801, USA

Contact Information

*Corresponding author. Email address: gunderhi@illinois.edu.

Keywords: liver tissue engineering; microwells; 3D cell culture; mechanobiology; microtissues; stem cells

Abstract

Investigating the role of mechanical signaling on stem and progenitor cell differentiation in three-dimensional (3D) microenvironments is key to fully understanding these processes. Towards this, we implemented a hydrogel microwell based method to produce arrays of multicellular microtissues in constrained geometries, which cause distinct profiles of mechanical signals in 3D. We applied this platform to a model liver development system to investigate the impact of tissue geometry and mechanical stress on liver progenitor cell bipotential differentiation into hepatocyte-like and biliary-like cells. We fabricated 3D liver progenitor cell microtissues of varied geometries, including cylinder and toroid, and used image segmentation on confocal images to track individual single cell phenotype within defined spatial coordinates. These studies demonstrated patterning of hepatocytic differentiation to the outer shell of the cylinder and toroid microtissues, except at the inner diameter surface of the toroid tissues. Biliary differentiation was distributed throughout the microtissue interior regions and was additionally increased in toroid tissues compared to cylinder tissues. We used finite element modeling to predict stress distributions in these microtissues which demonstrated that cell-cell tension correlated with hepatocytic fate, while compression correlated with decreased hepatocytic differentiation and increased biliary differentiation. Overall, this combined approach that integrates microscale fabrication, imaging and analysis, and mechanical modeling serve as a demonstration of how microtissue geometry can drive patterning of mechanical stresses that regulate cell differentiation trajectories. It also can serve as a platform for the further investigation of tissue morphogenetic signaling mechanisms in the liver as well as other stem cell differentiation contexts.

Introduction

The differentiation and morphogenesis of progenitor cells into functioning tissues is orchestrated through a diverse set of biochemical cues from neighboring cells and other elements of microenvironment. Mechanical force and mechanical signaling have been established as key to stem cell development and tissue behavior [1, 2]. Much of the work relating stem cell behavior to mechanical conditions, such as stiffness, geometry, and cell generated force, has been constrained to two-dimensional culture systems. Three-dimensional culture is more representative of in vivo conditions owing to increased cell-cell interactions and freedom for motility and reorganization, which are especially important in differentiation and morphogenesis. Compared with those on 2D, cells in 3D experience distinct mechanical stresses which influence their biological functions in embryonic development and tumor growth [3-5]. As 3D culture platforms have become more widely utilized, those that more specifically address mechanical loading and signaling have also been developed [6-8].

Since basic parameters, such as size, can affect cell and aggregate behavior [9], careful engineering is required to investigate cell response to a 3D environment. Microwell based platforms have emerged as a method to create large numbers of replicate multicellular structures for use in drug screening, disease modeling, and stem cell culture [10-15]. Platforms involving ECM protein or hydrogel encapsulation have been used to demonstrate that geometry of an embedded 3D tissue can drive tube morphogenesis and cancer invasion through endogenous stress patterns [16, 17]. Other systems, utilizing collagen encapsulated tissues constrained by mechanically tuned pillars, have shown patterns of ECM protein organization in response to mechanical stress [18, 19]. Microwell systems, without an encapsulating matrix, have been suitable for engineering the mechanical condition as cell derived forces responding to the constraining geometries were sufficient to cause alignment of ECM proteins [20].

Implementation of 3D systems with mechanical constraints to more tissue specific contexts, such as stem and progenitor cell development has been more limited. One system of interest is development of the liver. In the embryo, the hepatic diverticulum is comprised of bipotential progenitor cells, also referred to as hepatoblasts. These cells are capable of differentiation into either hepatocytes or biliary epithelial cells, also called cholangiocytes, and eventually establish the well described repeating lobule structure of the liver. The process of fate specification and eventual morphogenesis of liver tissue and bile ducts occurs in a spatially and temporally orchestrated process in the region immediately surrounding a portal vein, guided by a diverse set of cues. Hepatocytic fate is primarily associated with signaling through Wnt, HGF, and FGF [21-23] while biliary fate is linked to Notch and TGFβ activity [24-26]. Additional evidence shows that elements of the microenvironment such as ECM protein composition and stiffness further influence differentiation [27, 28]. We recently characterized the relationship between increased cell to surface traction force with increased biliary differentiation, highlighting the importance of mechanical signaling in this process [29]. The traction force distribution was a consequence of the monolayer geometry, demonstrating the relationship between geometry, mechanical loading, and cell behavior, an attribute that has been exploited in other 2D stem cell culture systems [30-37]. As in other systems, 3D culture of liver tissue is more physiologically relevant. However, the relationship between mechanical signaling and liver progenitor fate specification in 3D has not yet been characterized.

In this work, we implement an ECM-scaffold-free, hydrogel microwell based method to produced arrays of liver progenitor cell microtissues. The tissues have defined 3D geometries, including cylinders and toroids, with dimensions comparable to those of the liver lobule. These geometries also vary the predicted stress distributions. Using a single-cell image-segmentation-based approach, we characterize the 3D patterns of hepatocytic and biliary

differentiation in the various tissue geometries. We implement a finite element method model to predict the stress conditions of different regions of the tissues to investigate how tensile and compressive stress correlate with progenitor cell fate. We also explore the dependence of this pattern on cell contraction. Our findings provide additional evidence that mechanical signaling plays a role in the 3D spatial patterning of progenitor cells in liver development. These findings highlight the importance of considering tissue geometry and resulting stress condition in 3D culture platforms used to study stem cell behavior.

Materials and Methods

Wafer and PDMS mold fabrication

The master wafer was prepared using soft lithography techniques [38, 39]. A photomask was drawn in AutoCad and printed on to transparent plastic (CAD/Art services) which contained arrays of the desired geometries. A thin layer of negative photo resist (KMPR) was spin coated on to a clean 4” silicon wafer, and flood exposed to UV through the photomask. Following development, the exposed features were etched with deep reactive ion etching (STS Pegasus, SPTS Technologies) to a depth of approximately 200 µm.

For PDMS mold fabrication, a sheet of PDMS was first molded between two glass slides using a 500 µm spacer. 6 mm diameter holes, large enough to surround the feature arrays, were punched into the sheet. It was then treated with oxygen plasma and incubated with Trichloro(1H,1H,2H,2H-perfluorooctyl)silane vapor under vacuum for at least one hour. The sheet was positioned over the master wafer such that the holes aligned with the feature arrays to be molded. PDMS was poured over the wafer and sheet, fully degassed, and cured at 70 C for at least 3 hours. After curing, the 500 µm sheet was carefully peeled from the rest of the cured PDMS leaving 500 um raised platforms, which create to the loading well, on top of which

the feature arrays protrude an additional ~200 um. The two-step PDMS molding technique enables creation of multiple mold levels without requiring additional photolithography or etching steps. Additionally, a PDMS sheet was molded between glass slides using a 1 mm spacer. This sheet was cut into individual gasket pieces, each with a 7 mm hole.

Preparation of micro molded PEG substrates

Polyethylene glycol (PEG) hydrogels substrates were prepared by adapting previous protocols [10-12, 40]. 12 mm circular coverslips were immersed in 0.1 N NaOH for 1 hour, rinsed with DiH2O and placed on a hot plate at 110°C until dry. The NaOH treated coverslips were activated by immersion in 2% (v/v) 3-(trimethoxysilyl)propyl methacrylate in ethanol and placed on a shaker for 30 min. The activated coverslips were immersed in ethanol on the shaker for 5 min and again dried on a hot plate at 110°C. A 111.11 mg/mL 10kDa 4-Arm PEG-acylate (Laysan Bio) prepolymer solution was prepared in 1x PBS. This solution was mixed with Irgacure 2959 (BASF) solution (100 mg/mL in methanol) at a volumetric ratio of 9:1 (prepolymer:Irgacure) to achieve a final PEG concentration of 100 mg/mL. The solution was then degassed under vacuum.

For PEG molding, the 1 mm gasket was positioned around the feature array to be used, leaving approximately 1 mm between the raised platform and the gasket. A 50 µL droplet of prepolymer solution was deposited on the mold. A pipette tip was used to spread the prepolymer solution across the mold and knock bubbles from the mold features. The droplet was covered with an acrylate coverslip, which was lightly pressed against the gasket. The assembly was exposed to UV light using a Spot UV Curing System (OmniCure S1500, Excelitas Technologies) with a 320-390 nm Filter and adjustable collimating adapter, at an intensity of approximately 50 mJ/cm^2 for 30-60 seconds. The coverslip was then carefully removed from the mold and immersed in PBS in a 24 well plate. Prior to use in culture, the substrates were

sterilized by immersion in PBS supplemented with 1% (v/v) pen/strep under UVC for 30 minutes.

Cell culture and tissue formation

The experiments utilized BMEL 9A1 cells of passages between 28 and 34. BMEL cells were cultured as previously described [41]. For expansion, cells were thawed onto tissue culture plastic flasks coated with collagen I (0.5 mg/ml) and incubated at 37°C and 5% CO_2. For subculturing, flasks were treated with trypsin-EDTA (0.25% [v/v]) for ≤10 min to detach cells and replated on collagen I coated flasks. Growth media, for expansion, consisted of RPMI 1640 + GlutaMAX (Life Technologies, 61870-127) with fetal bovine serum (10% [v/v], FBS), penicillin/streptomycin (1% [v/v], P/S), human recombinant insulin (10 µg/ml, Life Technologies, 12585-014), IGF-2 (30 ng/ml, PeproTech, 100-12), and EGF (50 ng/ml, PeproTech, AF-100-15).

For tissue formation, cells were collected and resuspended to ~10 E6 cells/mL in differentiation media. A 50µL drop of cell suspension was added to the recessed loading well of each substrate. The 24 well plate was then centrifuged to drive cells into the wells. Excessed cells were removed by repeated media rinses. Tissues were cultured in differentiation media at 37°C and 5% CO_2 for 72 hours with a media change after the initial 24 hours. Differentiation media consisted of Advanced RPMI 1640 (Life Technologies, 12633-012) with FBS (2% [v/v]), P/S (0.5% [v/v]), L-glutamine (1% [v/v]), and minimum non-essential amino acids (1% [v/v], Life Technologies, 11140-050).

Growth factor and drug treatments

All growth factors and drugs were prepared and reconstituted according to the instructions of the manufacturers: EGF (50 ng/ml, PeproTech, AF-100-15) # mg/mL in PBS with 1% w/v BSA; (-)-blebbistatin (Cayman Chemical, 13013), 1 mg/ml in dimethyl sulfoxide

(DMSO); Y-27632 (Enzo Life Sciences, 270-333-M005), 5 mg/ml in deionized water (DiH_2O). Drugs were added to differentiation media at the following concentrations: (-)-blebbistatin, 25 µM; Y-27632, 15 µM. In experiments with addition of soluble treatments, these were added immediately after the excess cell media rinses. Media and treatments were refreshed after the initial 24 hours.

Immunocytochemistry

Cells were treated with brefeldin A (10 µg/ml, R&D Systems, 1231/5 in differentiation media) for 2 h prior to fixation by immersion in paraformaldehyde (4% [v/v] in 1× PBS) for 30 min at room temperature. Fixed samples were permeabilized by immersion in Triton X-100 (0.5% [v/v] in 1× PBS) for 1 hour at room temperature. Samples were incubated in blocking buffer (5% [v/v] donkey serum in 1× PBS) for 1 hour at room temperature. Primary antibody solutions were prepared by diluting one or more of the following antibodies in blocking buffer: mouse anti-HNF4a (1/200 from stock, Abcam ab41898), goat anti-OPN (1/60 from stock, R&D Systems, AF808), goat anti-Ecadherin (1/50 from stock, R&D Systems AF748), Acti-stain 488 phalloidin (7/1000 from stock, Cytoskeleton PHDG1-A). A 50 µL droplet of primary antibody solution was added to the recessed loading well of each substrate. Samples were incubated overnight at room temperature on a shaker. Samples were rinsed via 3 x 15-minute washes in PBS on a shaker. Secondary antibody solutions were prepared by diluting one or more of the following secondary antibodies in blocking buffer: DyLight 550-conjugated donkey anti-mouse IgG (1/50 from stock, Abcam, ab98767) and DyLight 488-conjugated donkey anti-goat IgG (1/50 from stock, Abcam, ab96935). A 50 µL droplet of secondary antibody solution was added to the recessed loading well of each substrate. Samples were incubated overnight at room temperature on a shaker. Samples were rinsed via 2 x 15-minute washes in PBS on a shaker.

Samples were incubated in DAPI solution (Invitrogen D1306) for 1 hour, and briefly rinsed in PBS.

A droplet of liquid mountant (ProLong™ Diamond Antifade, Initrogen) was added to each substrate, and the coverslips were mounted onto standard microscope slides. Mounted samples were cured for at least 24 hours at room temperature. Once cured, samples were sealed with clear nail polish.

3D Tissue Imaging, Segmentation, and analysis

The fluorescently stained samples were imaged using a laser scanning confocal microscope (Leica TCS SP8). 3D image stacks were segmented into individual cells using an adaptation of the MINS (modular interactive nuclear segmentation) MATLAB/C++-based segmentation platform [42] on the nuclear image (DAPI) channel. Utilizing the Bio-Formats software tools [43], the microscope software generated .lif files were directly loaded into the software to sequentially segment all image stacks from each tissue array, and automatically read in metadata such as pixel size.

Semi-automated post processing and analysis was completed using a series of MATLAB scripts. First, an edge detection-based process was used to identify the outer tissue boundary in each image slice to mask out cells and debris not incorporated into the tissue. Due to nature of the microwells, tissues can move and rotate in all three dimensions, thus rotation and alignment is required to compare spatial behavior across replicate tissues. For this, a best fit ellipse was fit to the XZ, YZ, and XY projections of the masked, segmented nuclei data. The orientations of the best fit ellipses were used to rotate the nuclei centroids such that major axes from the XZ and YZ projections were aligned with the horizontal (X) and vertical axis (Y) respectively, the major axis of the XY projection was aligned to the horizontal (X) axis. The nuclei were also translated such that tissue center is at the origin. The major and minor axis of

the XY projection were used to normalize the X and Y coordinates, and the height of the tissue was used to normalize the z coordinates. This normalized coordinate system was used in subsequent analysis to enable spatial comparison across replicates independent of slight differences in tissue size after cell aggregation.

For OPN and HNF4a expression analysis, the average intensity of the relevant stains was calculated in each of the segmented nuclei, along with intensity of the surrounding 3D area. The difference between the intensities and the surrounding background were used for analysis to account for intensity difference due to imaging penetration across the thickness of the tissue. A two component gaussian mixture model was applied to these relative intensities within each tissue to sort tissues into positive or negative for each stain.

For phenotype heat map generation, cells from replicate tissues were binned in 2D according to the relevant normalized coordinates, and the percentage of cells within each bin positive for the strain was calculated. For 1D plots, normalized shell and radial coordinates were calculated as described in Supplementary Figure S3. For region-based box plots, regions were separated based on normalized radial and shell coordinates as shown in Supplementary Figure S3.

For e-cadherin and actin heat map generation, the corresponding images were rotated and centered using the segmented nuclei projection best fit ellipses as described earlier. Images were down sampled by a factor of 4, the XYZ coordinates for each remaining voxel were calculated, and coordinates were normalized using the best fit ellipses. Normalized XY were coordinates were converted to normalized radial coordinate. Voxels were binned into a triangle mesh, and the average intensity in each mesh unit was calculated. This was repeated across multiple tissues using the same mesh to generate an average heat map.

Finite element modeling

3D Tissue geometries were drawn in Autodesk inventor with dimensions that approximate measured final tissue dimensions. Separate solid bodies were generated for each material type in the tissue model. These geometries were exported as STEP or IGES files. The finite element mesh generator software Gmsh was used to generate tetrahedral mesh files for each CAD geometry [44]. The finite element model was produced using the FEBio software suite [45]. The PreView software was used to import the geometry, set boundary conditions, and specify material properties. Tissues were modeled as a union of bodies with each body being assigned a material [46]. The core and intermediate regions were modeled as Neo-Hookean solids. The free outer shell and pillar contacting shell regions were modeled as solid mixtures of a Neo-Hookean material and material with a prescribed isotropic active contraction. Due to the actual stiffness of the tissues being unknown, non-dimensional stiffness and prescribed contraction values were used to analyze the relative stress patterns arising from parameter choices. Intermediate, outer shell, and pillar-contacting shell regions were assigned a Young's modulus of 1. The core Young's modulus was set to 0.5. The outer shell and pillar contacting regions' prescribed stress was set to 5. Because the PEG substrate is much stiffer than the tissue, the microwell boundaries and pillars were either modeled as rigid material with a sliding contact, or a boundary condition preventing displacement normal to the surface. The simulation was run using the FeBio solver as a steady-state static single time point using default settings. Simulation results were visualized in the PostView program, which was also used to export results as a VTK file. Paraview [47] was used to calculate principle stresses, visualize data, and generate figures.

Microgel force sensor experiments

For microgel force experiments, the micowell substrates were fabricated on a glass bottom 35 mm dish (Cell E&G, GBD00003-200). Alginate microgels with fluorescent particles were fabricated as previously described with 0.5% w/v alginate [5]. The droplet suspension was mixed with the cell suspension just before seeding the microwells. Alginate is not stable in RPMI medium. Therefore, in microgel experiments, differentiation media was altered to use Advanced DMEM (Gibco 12491-023) instead of advanced RPMI. Images were acquired using a laser scanning confocal microscope (Leica TCS SP8). Microgels were first located and a low zoom image was collected to be able to mark the XY location of the particle within the tissue. Images of the stressed elastic round microgels were collected, and the tissues were treated with 2.5% Triton X-100 detergent to obtain stress-free conditions. Images of the particles were collected ever 5-10 minutes for approximately 1 hour until the stress-free condition was achieved. ImageJ was used to measure the diameter and centroid location of the tissues and the location of the microgel. 3D confocal images were deconvolved (AutoQuant X3), and the volume was measured using MATLAB scripts. Average compressive stress was calculated based on the Poisson's ratio of 0.4 and the bulk modulus of 3012 Pa, from interpolation of previous alginate bead stiffness measurements [5].

Statistical analysis

Experiments consisted of three or more biological replicates with multiple tissues per experiment. For percent positive heat map generation, all cells from all replicate tissues in the shown condition were binned in a 50 by 50 RZ space, percent of cells positive for each marker was calculated at each bin location and plotted. For region-based calculations, the percent positive cells in each region for each individual tissue was calculated and plotted. For line plots, the cells in individual tissues were binned in the relevant coordinate space, and a percent

positive for the marker was calculated for each bin from each individual tissue. Line plots represent the mean percent positive for each bin position across replicate tissues with the 95% CI ribbons in gray. Line and box blots were generated using the ggplots2 package for R [48, 49]. For hypothesis testing, Welch's two-sample t-test was performed using the base t.test function in R. $P<0.05$ was considered significant. P-values are indicated in the figures.

Results

Micromolded PEG substrates generate 3D microtissue with defined geometries

We implemented a microwell based approach to generate arrays of bipotential mouse embryonic liver (BMEL) cell three-dimensional tissues with defined geometries. For fabrication, a master wafer was prepared using photolithography and etching (Supplementary Fig S1A). Initial trials using single level PDMS molds required large volumes of high-density cell suspension, limiting the tissues that could be produced. This motivated incorporating a loading well similar to the seeding chamber provided by other available molds, which are produced by 3D printing rather than standard soft lithography [11].To achieve a multilevel mold without additional lithography steps or other equipment, we first fabricated a 500 µm PDMS gasket sheet with an array of holes large enough to surround each sub-array of features. We passivated the gasket with a fluoro-silane. The gasket sheet was positioned over the wafer before addition of the PDMS (Fig 1A). After curing, the PDMS was removed from the wafer, and the gasket sheet was peeled from the rest of the PDMS producing the two-level mold (Supplementary Fig S1B).

For substrate fabrication, a prepolymer solution consisting of 100 mg/mL 4-Arm-PEG-Acrylate (Laysan Bio) and 10 mg/mL photoinitiator (Irgacure 2959, BASF). A 1 mm thick PDMS gasket was positioned around the feature (Fig 1B, Supplementary Fig S1C). A droplet of the

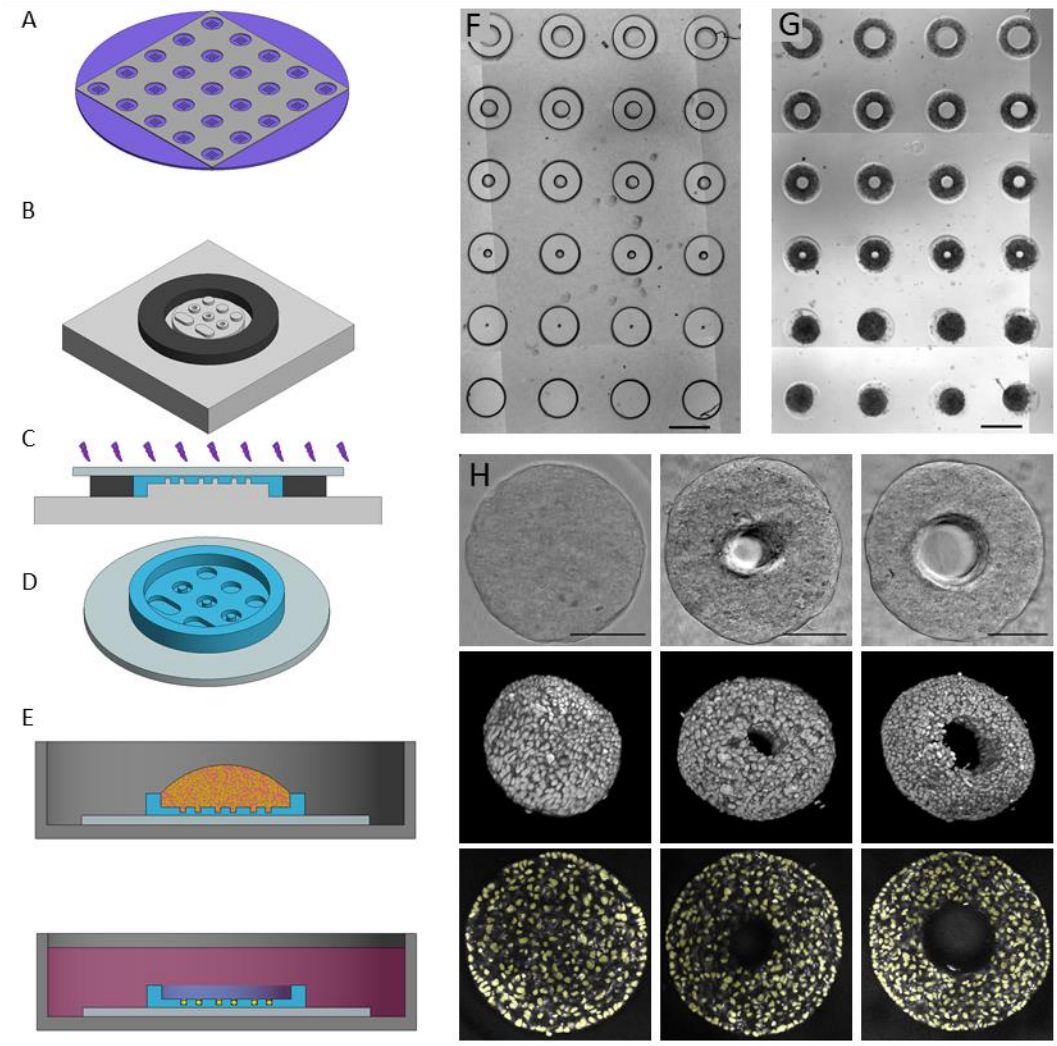

Figure 1. Micromolding-based process for microwell and tissue fabrication, and image analysis processes. A) A master wafer, prepared via photolithography and DRIE etching, is fit with a passivated PDMS gasket. PDMS is cured on the wafer to produce molds. B) A circular gasket is fit around the mold region of interest. C) The prepolymer solution is added to the mold, an activated coverslip is pressed on the droplet, and it is polymerized with UV light. D) Rendering of hydrogel substrate. E) For tissue seeding, a drop of cell suspension is added to the inset region of the substrate. Following centrifugation, excess cells are removed, and cells condense into aggregates. F) Brightfield image of a section of a PEG substrate with an array of microwells with equal cross-sectional area. G) Bright field image of an array of tissues. H). Top: Brightfield images of cylinder tissues (left), and toroid shaped tissues of varied inner diameter (middle and right). Center: 3D renderings of confocal images of nuclei distribution in tissues. Bottom: Nuclei image segmentation overlaid on central confocal image slices of tissues.

prepolymer solution was placed over the PDMS mold, a 12 mm acrylate functionalized coverslip was floated over the droplet, and the assembly was exposed to UV (Fig 1C). The coverslip was removed from the mold, resulting in a PEG substrate with 500 um side walls, with an inset array of microwells approximately 200 µm deep (Fig 1B, Supplementary Fig S1). This approach enables a wide variety of well geometries with high aspect ratio features, such as cylinder and toroid wells of varied inner and outer diameter (Figure 1D). In this example, the inner post diameter ranges from 50 to 250 um, and the outer diameter is adjusted such that all wells have the same cross-sectional area as a 400 µm diameter circle. This approach aims for tissues with approximately the same initial number of cells across the geometries. When measured optically, well dimensions closely reflected those drawn in CAD for the photomask (Supp Figure 1A, B).

For tissue fabrication, the substrates coverslips were placed into 24 well plate wells and sterilized with UV light. A droplet of cell suspension (~10 E6 cells/mL) was placed in the loading well of each substrate. The plates were centrifuged driving cells to completely fill the microwells. Excess cells were removed with media washes (Fig 1E). Because the microwells were non-fouling and non-adhesive, cells only adhered to themselves, and aggregated into dense, 3D tissues constrained by the wells. In cylindrical wells, the cells aggregate and condense into a roughly cylindrical tissue. In the toroid microtissues, the cells aggregate and condense away from the outer walls, but around the central post, resulting in roughly donut shaped tissue (Fig 1G,H). Confocal images highlight the 3D structure of the microtissues (Fig 1H). After 72 hours in culture, the mean diameter of tissues in 400 µm diameter wells was 226 µm. the mean diameter of condensed tissues in toroid wells with 150 µm diameter posts, was 286 µm (Supplementary Fig S1G). Subsequent references to toroid and cylinder microtissues describe these two geometries unless otherwise noted. We used image segmentation [42] to identify

and locate individual nuclei to enable single cell analysis in 3D (Fig 1H,). We observed that despite the equal cross-sectional area, the mean final number of cells incorporated into cylinder tissues was higher than that in and toroid tissue, at 3498 and 2841 respectively (Supplementary Fig S1F).

Hepatocytic and biliary phenotype patterning in cylindrical microtissues

After 72 hours of culture, microtissues were fixed and immunostained for the biliary marker osteopontin (OPN) and hepatocytic marker HNF4a. In tissues produced from 400 µm diameter cylindrical wells, cells expressing OPN were sparsely distributed throughout the tissue, while HNF4a expressing cells were almost exclusively found at the outer shell of the tissues (Fig 2A, B, Supplementary Fig S2). To quantify this behavior across microtissues, we implemented an image segmentation based single cell analysis pipeline to determine cell phenotype and location in a coordinate system normalized by the tissue radius and thickness (Supplementary Fig S3A). We mapped the percentage of HNF4a and OPN positive cells across a normalized radial and Z coordinate (RZ) space from replicate (N = 45) tissues, taking advantage of the rotational symmetry. This revealed consistent spatial patterning of HNF4a positive cells at the outer surface of the tissues (Fig 2D). Here, OPN positive cells were distributed across the cross section, with some exclusion from the outer region (Fig 2G).

The condensed tissues adopt a final shape with a circular XY cross section, and a more ovular RZ cross section, which can be approximated as a rectangle with semicircular caps (Supplementary Fig S3B, C). Based on this approximation, we calculated a normalized shell coordinate to describe cell position with a single dimension (Fig 2C, Supplementary Fig S3D). Plotting percentage of HNF4a positive cells versus this coordinate further highlighted the outer surface patterning of HNF4a positive cells (Fig 2F). Plotting percentage of cells positive for OPN versus this coordinate revealed the decrease in OPN positive cells at the outer surface,

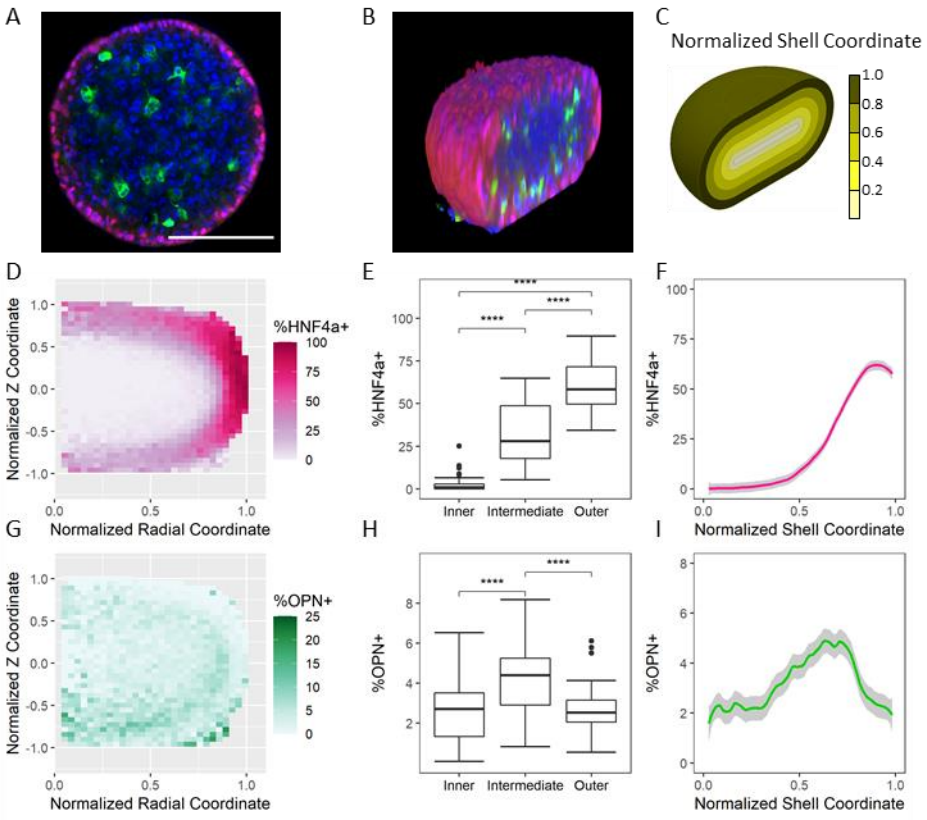

Figure 2. Spatial patterning of Hepatocytic and biliary differentiation in cylinder microtissues. A) XY confocal slice of a representative cylinder microtissue stained for hepatocytic marker HNF4a (red), biliary marker OPN (green), and with DAPI (blue). Scale bar 200 µm B) 3D rendering of confocal image stack, sliced across the approximate center XZ plane. C) Schematic view of the normalized shell coordinate. D) Percentage of HNF4a positive cells in RZ space from N=45 tissues. E) Percentage of HNF4a positive cells in the Inner, Intermediate, and Outer regions. F) Percentage of HNF4a positive cells versus normalized shell coordinate, mean ± 95% CI shown in gray. G) Percentage of OPN positive cells in RZ space. H) Percentage of OPN positive cells in the Inner, Intermediate, and Outer regions. I) Percentage of OPN positive cells versus normalized shell coordinate, mean ± 95% CI shown in gray. **** p <= 0.0001.

and a slight elevation in OPN positive cells just inside of the outer region (Fig 2I). Further, we sorted cells into an inner, intermediate, and outer region based on the shell coordinate (Supplementary Fig S3C) and calculated the percentage cells positive for each marker. We observed a statistically significant difference in percentage of HNF4a positive cells across all regions, with the outer region being the highest, and inner the lowest (Fig 2H). We observed a statistically significant increase in percentage of OPN positive cells in the intermediate region compared to the outer and inner regions.

Hepatocytic and biliary phenotype patterning in toroid microtissues

Like the cylindrical tissues, in toroid tissues, produced with wells with a 150 µm center pillar, OPN positive cells were sparsely distributed across the 3D structure while HNF4a positive cells were primarily found at the outer surface. However, low levels of HNF4a positive cells were observed at the surface contacting the PEG pillar (Fig 3A, B, Supplementary Fig S4). Plotting percentage HN4a positive cells in RZ space from replicate (N = 40) microtissues demonstrates this behavior is consistent across tissues (Fig 3G). Plotting percentage of OPN positive cells in RZ space revealed reduced OPN positive cells in the outer shell, but not at the region contacting the pillar. As the PEG pillar is chemically inert to the cells, this region would be expected to behave as the rest of the outer surface, implicating mechanical interactions in altering the differentiation behavior.

As with cylinder microtissues, we use the plane of radial symmetry define a normalized shell coordinate (Fig 3C, Supplementary Fig S5A, B). Plotting marker expression frequency in this space emphasizes that HN4a positive cells are most found at the outer region, and the percentage of OPN positive cells drops in this region (Fig 3E, I). This coordinate does not indicate proximity to the pillar contacting surface. Thus, we also plotted percentage of cells positive for each marker against normalized radial coordinate (Fig 3D). This revealed that the

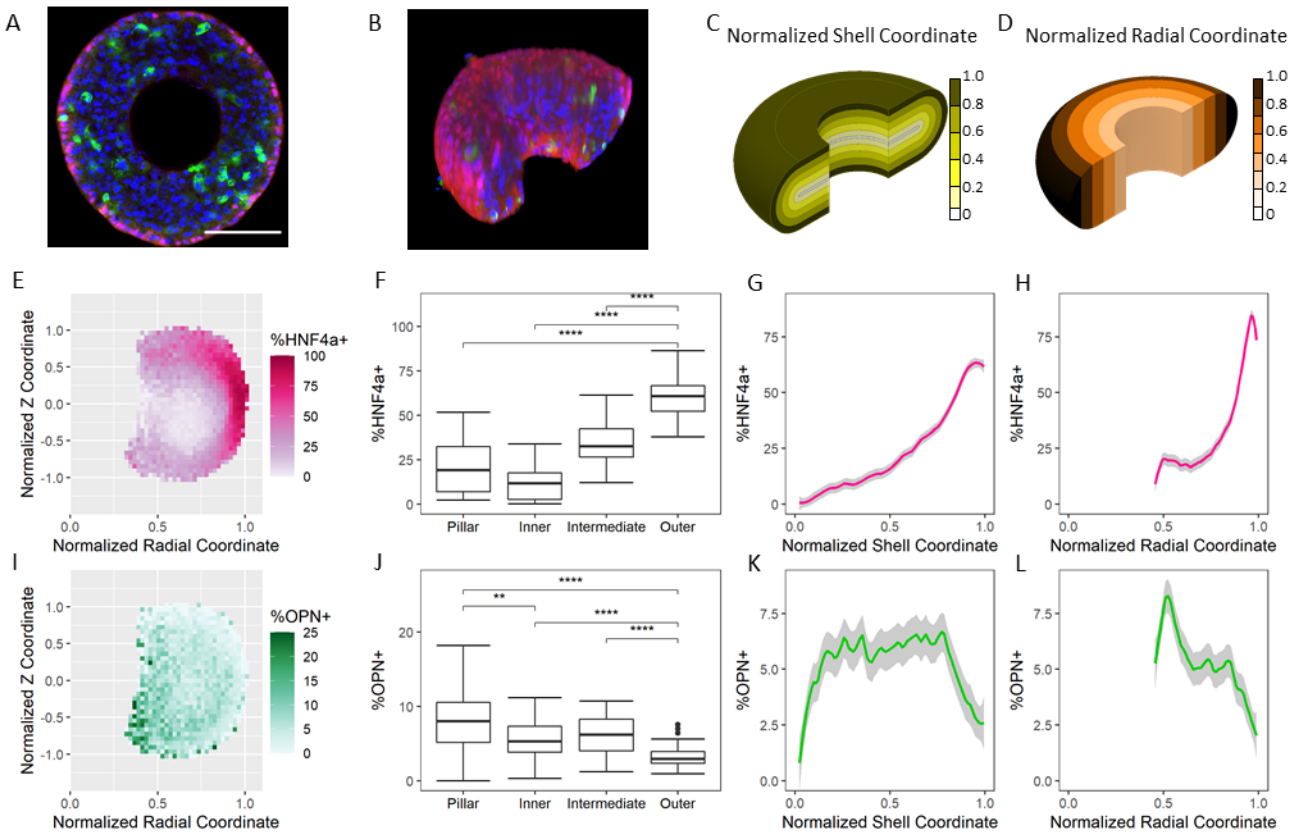

Figure 3. Spatial patterning of Hepatocytic and biliary differentiation in toroid microtissues. A) XY confocal slice of a representative toroid microtissue stained for hepatocytic marker HNF4a (red), biliary marker OPN (green), and with DAPI (blue). Scale bar 200 µm B) 3D rendering of confocal image stack, sliced across the approximate central XZ plane. C) Schematic view of the normalized shell coordinate. D) Schematic view of the normalized radial coordinate. E) Percentage of HNF4a positive cells in RZ space from N=40 tissues. F) Percentage of HNF4a positive cells in the Pillar, Inner, Intermediate, and Outer regions. G) Percentage of HNF4a positive cells versus normalized shell coordinate. H) Percentage of HNF4a positive cells versus normalized shell coordinate. Mean ± 95% CI shown in gray. I) Percentage of OPN positive cells in RZ space. J) Percentage of OPN positive cells in the Pillar, Inner, Intermediate, and Outer regions. K) Percentage of OPN positive cells versus normalized shell coordinate. L) Percentage of OPN positive cells versus normalized radial coordinate. Mean ± 95% CI shown in gray. ** $p <= 0.01$, **** $p <= 0.0001$.

percentage OPN positive cells increased near the pillar contacting surface, where R is approximately 0.4. Further, we used these two coordinates to sort cells into inner, intermediate, outer, and pillar regions (Supplementary Fig S5B). The percentage of cells positive for HNF4a was statistically significantly higher at the outer region compared to each other region, including the pillar. Percentage of OPN positive cells was lowest at the outer region. There was a small increase in percent OPN positive at the pillar compared to the inner region (Fig 3H).

Toroid shape and EGF increase biliary differentiation

Overall, untreated toroid microtissues had a statistically significant increase in percentage of OPN positive cells per tissue compared to cylinder tissues (Fig 4A). Treatment with EGF increased the percentage of OPN positive cells in both toroid and cylinder microtissues, while causing only a minor decrease in the percentage of HNF4a positive cells (Figure 4 A, B). As with untreated tissues, EGF treated toroid tissues showed an increase in percent OPN positive cells compared to EGF treated cylinder tissues. EGF treatment did not disrupt the spatial pattern of HNF4a positive cells. In both the cylinder and toroid geometries, HNF4a cells were mostly restricted to the outer surface. In the EGF-treated toroid microtissues, HNF4a positive cells were restricted from the pillar contacting surface (Fig 4C, D).

Along with amplifying overall expression of biliary marker OPN, treatment with EGF amplified the spatial pattern of OPN expression. Plotting OPN frequency in RZ space reveals that OPN frequency increases in the intermediate area, just inside the outer surface (Fig 4E). Using the normalize shell coordinate highlights that percent OPN positive is low at the outer shell, where HNF4a cell frequency is highest, peaks in the intermediate zone, and decreases moving towards the core (Fig 4 F). The pattern also holds true when using the radial coordinate (Fig 4G) This trend is confirmed when comparing percent OPN positive in the inner, intermediate, and core regions, as percent OPN positive is highest in the intermediate zone

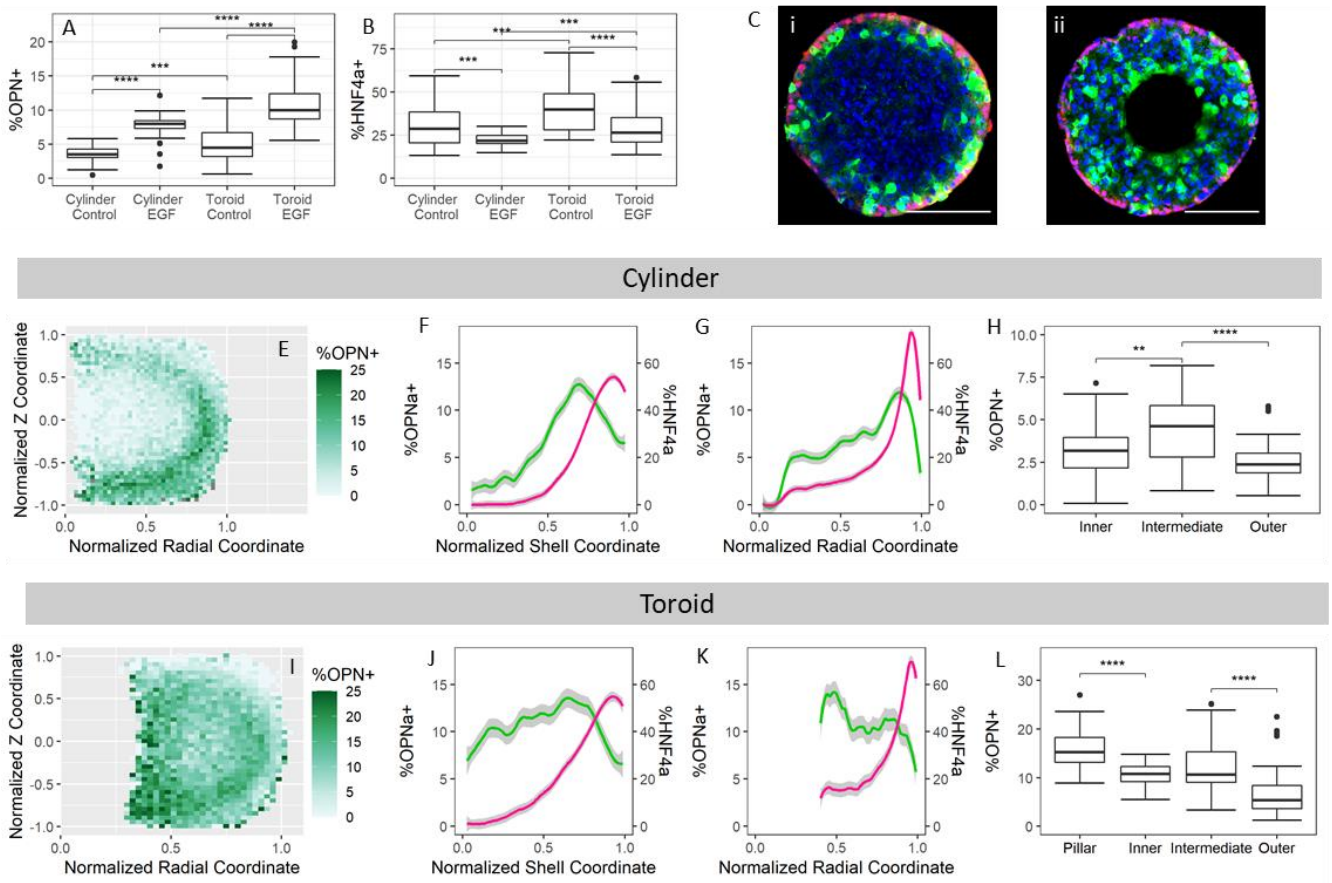

Figure 4. Hepatocytic and biliary differentiation in EGF treated BMEL microtissues. A) Percentage of OPN positive cells per microtissue by shape and treatment. Control is no treatment. B) Percentage of HNF4a positive cells per microtissue by shape and treatment. Control is no treatment. C) Confocal slice of a representative EGF treated cylinder (i) and toroid (ii) microtissue stained for HNF4a (red), OPN (green), and with DAPI (blue). Scale bar 100 µm. E) Percentage of OPN positive cells in RZ space from N=32 cylinder microtissues. F) Percentage of OPN (green) and HNF4a (magenta) positive cells versus normalized shell coordinate in EGF treated cylinder microtissues. G) Percentage of OPN (green) and HNF4a (magenta) positive cells versus normalized radial coordinate in EGF treated cylinder microtissues. Mean ± 95% CI shown in gray. H) Percentage of OPN positive cells in the Inner, Intermediate, and Outer regions of EGF treated cylinder microtissues. I) Percentage of OPN positive cells in RZ space from N=44 toroid microtissues. J) Percentage of OPN (green) and HNF4a (magenta) positive cells versus normalized shell coordinate in EGF treated toroid microtissues. K) Percentage of OPN (green) and HNF4a (magenta) positive cells versus normalized radial coordinate in EGF treated toroid microtissues. Mean ± 95% CI shown in gray. L) Percentage of OPN positive cells in the Pillar, Inner, Intermediate, and Outer regions of EGF treated toroid microtissues. ** p<= 0.01, ***p<=0.001, **** p <= 0.0001.

(Fig 4H). In toroid tissues, we see in the RZ space that percent OPN positive cells similarly increases in region just inside of the outer shell as well as near the pillar contacting region (Fig 4I). The increase in OPN cell frequency just inside of the outer shell is highlighted in the shell coordinate plot, where OPN cell frequency is low near shell coordinate of 1, where HNF4a cell frequency is highest. Percent OPN positive peaks near shell coordinate of 0.75. Plotting OPN cell frequency versus normalized radial coordinate shows the other peak in percent OPN positive, near the pillar the contacting region ($R \approx 0.4$). These two peaks are confirmed when comparing the percent OPN positive in the pillar, inner, intermediate, and outer regions (Fig 4L).

Increased E Cadherin expression colocalized with increased HNF4a positive cells

To further characterize the architecture of the tissues we stained tissues for actin and E-cadherin (ECAD) along with HNF4a. In cylinder microtissues, we observed an outer actin ring, visible in XY cross sections (Fig 5Ai, Supplementary Fig S6A). An actin ring similarly forms at the outer periphery in toroid microtissues, and at the inner, pillar contacting surface (Fig 5ii). ECAD was expressed at low levels throughout, but highest at the outer shell in both cylinder and toroid geometries (Fig 5A iii). In toroid microtissues, ECAD expression did not increase near the pillar contacting region (Fig 5A iv). Thus, the regions of increased ECAD expression correlated with the regions of increased HNF4a positive cells. Inspection of these regions with higher magnification confirmed these patterns and that the increased ECAD expression occurred at cell-cell junctions (Supplementary Fig S6A). To assess the consistency and 3D characteristics of this behavior, we averaged actin and ECAD stain intensity across the RZ plane of symmetry of the tissues and averaged this across multiple tissues. From this, we observe that the actin ring extends into an actin shell. Further, this confirmed the increased

ECAD expression in the outer shell region, coincident with the region of increased HNF4a positive cells (Fig 5B).

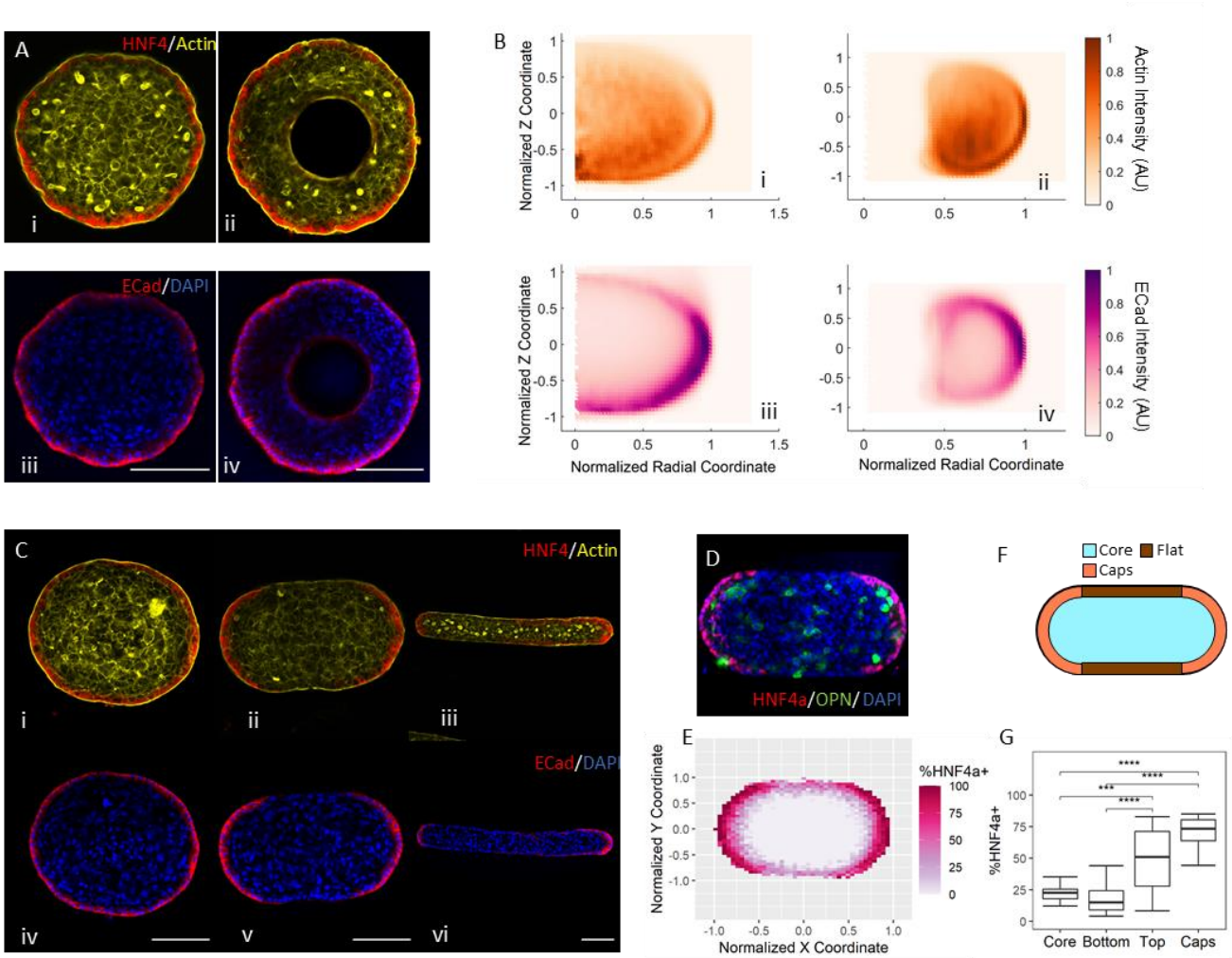

Figure 5. Patterning of actin, E-cadherin, and HN4a in 3D BMEL microtissues. A) Confocal image of a representative cylinder (i) and toroid (ii) microtissue stained for HNF4a (red) and actin (yellow), and with DAPI (blue), and a representative cylinder (iii) and toroid (iv) microtissue stained for ECAD (red) and with DAPI (blue). Scale bar 100 µm. B) Averaged actin intensity in RZ symmetry plane averaged from n = 8 (i) cylinder and (ii) toroid tissues in RZ space. Averaged ECAD staining intensity in RZ symmetry plane averaged from n = 8 (iii) cylinder and (iv) toroid microtissues. C) Confocal images of representative (i) 300 µm, (ii) 200 µm, and (iii) 100 µm wide oblong microtissues stained for HNF4a (red) and actin (yellow). Confocal images of representative (i) 300 µm, (ii) 200 µm, and (iii) 100 µm wide oblong microtissues stained for ECAD (red) and with DAPI (blue). Scale bar 100 µm. D) Confocal image of a representative 200 µm wide oblong microtissue stained for HNF4a (red), OPN (green), and with DAPI (blue). Scale bar 100 µm. E) Percentage of HNF4a positive cells in RZ space in the center 25% of the tissue height from N=18 200 µm wide oblong microtissues. F) Descriptive regions of oblong microtissues. G) Percentage of HNF4a positive cells in the core, flat, and regions of 200 µm tissues. ***p<=0.001, **** p <= 0.0001.

Hepatocytic differentiation excluded from flat regions of oblong microtissues

To further explore the relationship between geometry and differentiation, we prepared "oblong" microtissues using wells with a racetrack like cross section, a rectangle with semicircular caps. Here, the wells were designed such that the width was set to 100, 200, or 300 µm, and the length is chosen such that the cross-sectional area is equal to that of a 400 µm diameter circle. After 72 hours of culture, tissues in the 300 µm wide oblong wells condense into slightly elongated, ovular cylinders. In these geometries, the spatial patterns of actin, ECAD, and HN4a expression was like those observed in cylinder microtissues (Fig 5C i,ii). Microtissues in the 200 and 100 µm wide oblong wells condense such that they are pressed against the side walls, producing microtissues with flat sides and rounded caps. In these tissues, the cortical actin ring is present around the entire periphery of the microtissue cross section. However, HNF4a positive cells were generally found at the round cap regions, and less so at the flat, wall contacting sides. Areas of increased ECAD expression also followed this pattern (Fig 5 iii-vi, Supplementary Fig S6A).

To confirm this phenomenon, we stained for and quantified HNF4a positive cells in replicate 400 µm oblong tissues (Fig 5D). Plotting percent HNF4a positive cells in normalized XY space for the central 25% of the tissues' thickness showed that the oblong tissues consistently have higher levels HNF4a positive cells at the round caps than the flat sides, and HNF4a positive cells were infrequently found through the core (Fig 5E). Dividing the tissues into core, cap, and flat regions (Fig 5F), the caps have statistically significant higher levels of HNF4a positive cells than the flat and core regions (Fig 5G). Viewed in normalize XZ space, we observed that the top region of the tissues behaves similarly to the caps, while the bottom of the tissue behaved like the flat sides (Supplementary Fig S6C-F).

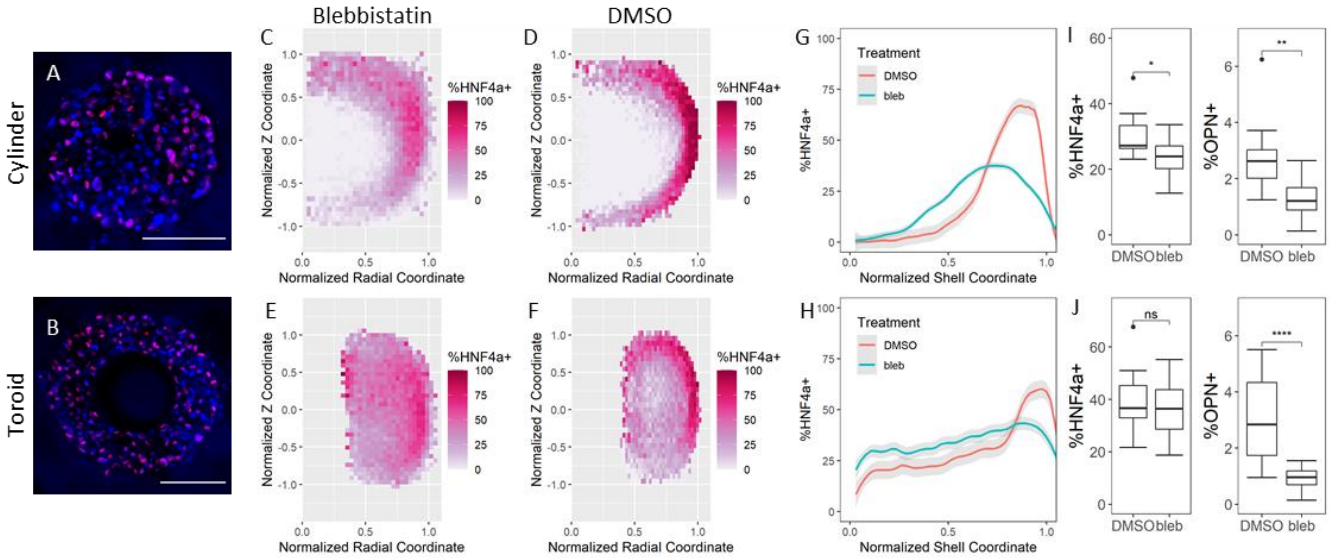

Figure 6 Disruption of hepatocytic patterning with blebbistatin. Confocal image the central slice of a representative cylinder (A) and toroid (B) blebbistatin-treated microtissue stained for HNF4a (red) and with DAPI (blue). Scale bar 100 µm. C-F) %HNF4a positive heat maps for DMSO and blebbistatin treated cylinder and toroid microtissues. G,H) %HNF4a positive versus shell coordinate for DMSO and blebbistatin-treated cylinder and toroid microtissues. Mean ± 95% CI shown in gray. I,J) Overall %HNF4a and %OPN positive cells per microtissues in DMSO and blebbistatin-treated cylinders and toroids. * p<= 0.05, ** p<= 0.01, **** p <= 0.0001.

Blebbistatin disrupts hepatocytic fate patterning and biliary and biliary differentiation

To investigate the role of actin-myosin contractility on differentiation in 3D, we treated microtissues with blebbistatin to disrupt actin-myosin contraction. Overall, treatment with blebbistatin reduced biliary differentiation in all geometries (Fig 6I), suggesting a role of cell contractility in biliary differentiation. In both cylinder and toroid microtissues, blebbistatin did not greatly affect overall levels of hepatocytic differentiation compared untreated or vehicle (DMSO) treated (Figure 6I) but did appear to disrupt the spatial pattern (Fig 6A, B). In the cylinder microtissues, there remained increase in HNF4a positive cells compared to the core, however this sorting was less pronounced in blebbistatin treated relative to DMSO treated microtissues (Fig 6C,D). Using the shell coordinate, we observed that the peak level of HN44a positive cells was reduced and spread further into the structure (Fig 6G). Blebbistatin was even more disruptive to the spatial patterning in toroid microtissues (Fig 6E,F). The peak level HNF4a positive cells were more uniformly distributed across the microtissue volume (Fig 6H). Treatment with ROCK inhibitor Y-27632 did not impact the overall frequency or spatial pattern of biliary or hepatocytic differentiation in cylinder or toroid microtissues (Supplementary Figure S7).

Mechanical models suggest differing regions of compression and tension from cell contraction

To understand the mechanical behavior of the microtissues, we implemented a 3D finite element method (FEM) based model, building off of previously reported 2D and 3D tissue models (Supplementary Fig S8) [34, 46, 50]. Based on the actin and ECAD patterns observed, we modeled the microtissues as having a contractile shell, similar to that described in the aggregates produced and characterized by Lee et. al. [46]. Based on the increased OPN positive cell frequency in the region just inside the outer shell, we modeled the intermediate region as stiffer than the core, also as suggested by Lee et. al. [14] (Supplementary Fig 7A).

The results of this model suggested that in the cylindrical microtissue, the outer shell region was primarily under tension, with positive first and second principle stresses, and third principle stress of approximately zero. The intermediate and core regions were entirely in compression, which the largest compressive stress in the intermediate region (Fig 7F, G, Supplementary Fig S9B). In the toroid microtissue model, the contractile shell region is also primarily under tension, and the intermediate and core regions were entirely in compression, with increased compression at the intermediate region. However, the pillar contacting region is experiencing compression at comparable levels to the intermediate zone (Figure 7H, I, Supplementary Fig S9B).

To validate some of the results of this model, we imbedded alginate microgels into the microtissues, which contained fluorescent beads, to measure forces within the tissue. In these experiments, an image is acquired of the microgel under the stress of the tissue. The tissue is lysed with a detergent, and an image is collected of the relaxed (stress-free) microgel. The relative displacement of the fluorescent beads can be used to measure the cell forces of the microgel [5]. These microgels were successfully incorporated into both cylinder and toroid microtissues (Fig 7A). Visual inspection of the microgels before and after lysing revealed microgels frequently expanded upon relaxation, indicated they had been in compression. To assess this behavior, we measured the volume of the microgel before and after lysing. We then calculated the relative volume change and calculated the average compressive stress in each microgel. All measured microgels in both tissue geometries expand upon tissue lysing, indicating they were in compression. This confirmed the compression in the interiors of the tissues. The average compressive stress across replicate cylinder and toroid tissues was 695 ± 197 Pa and 590 ± 207 Pa respectively, however we did not observe a statistically significant difference in average compressive stress between toroid and cylinder tissues or as a function

of radial position (Fig 7B). More dense distributions of microgels in toroid and cylinder tissues may be needed for studies in the future.

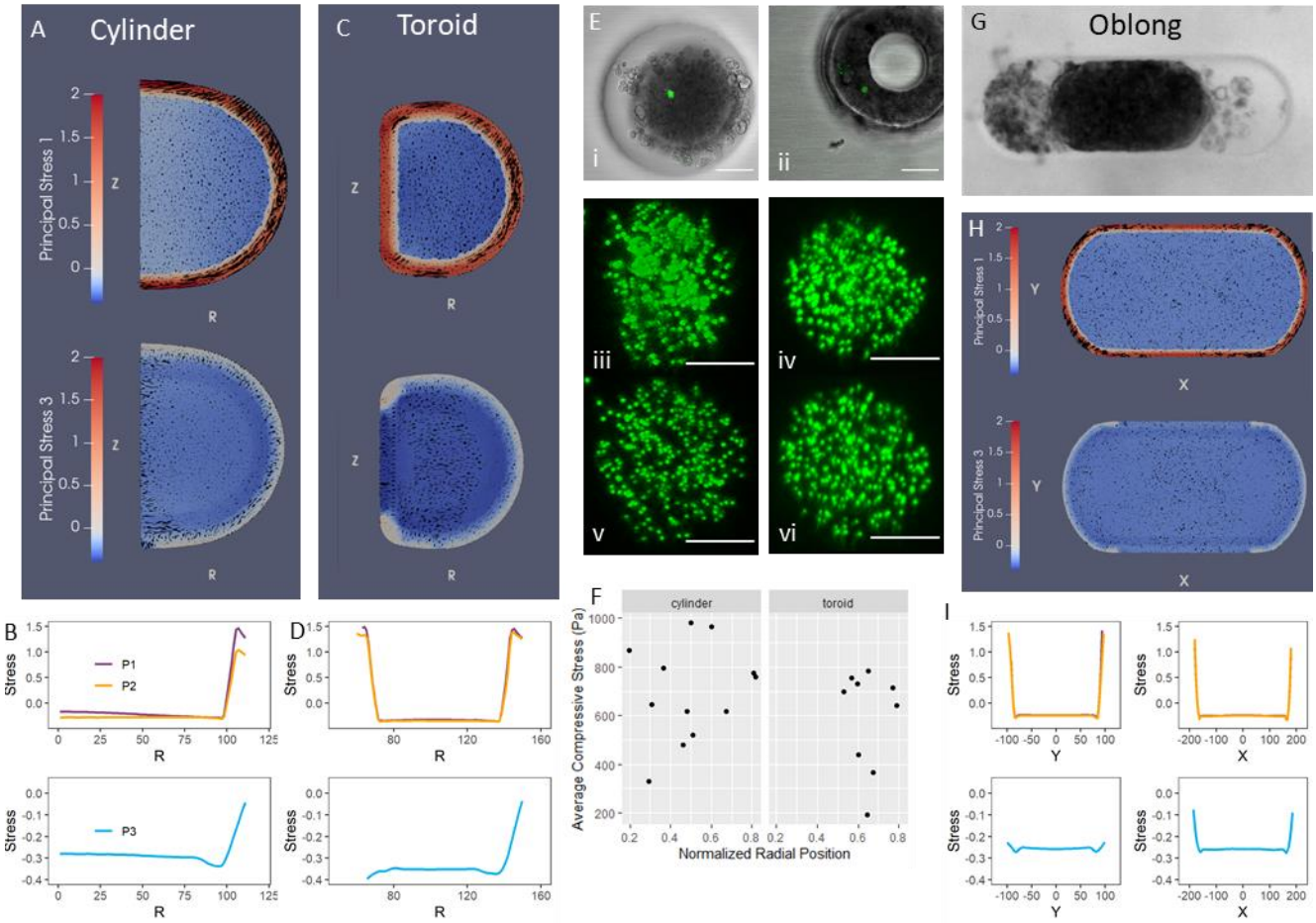

Figure 7. Modeling and measurement of stress in 3D BMEL microtissues. A) Simulated first and third principal stresses for an RZ slice of a representative cylinder microtissue. B) Simulated principal stresses at the line of Z = 0 from the above RZ slice (cylinder). C) Simulated first and third principal stresses for an RZ slice of a toroid microtissue. D) Simulated principal stresses at the line of Z = 0 from the above RZ slice (toroid). Stress values given in relative, arbitrary units. E) Representative cylinder (i) and toroid (ii) microtissues with an embedded microgel. Scale bar 100 um. Maximum intensity projections of the stressed (iii and iv) and relaxed (v and vi) microgels from the cylinder and toroid geometries shown above. Scale bar 10 um. F) Average compressive stress on microgels in cylinders and toroids plotted versus radial position. G) Brightfield image of an oblong microtissue. H) Simulated first and third principal stresses from the central XY slice of an oblong microtissue. I) Simulated principal stresses at the line of X = 0 (left) and Y = 0 (right) from the above XY slice (oblong).

We next applied the FEM model to the oblong microtissues. After 72 hours of culture, the tissues continue to contact the long flat walls (Fig 7E). While this may be expected to occur during aggregation, under uniform contraction the tissue would be expected to uniformly shrink away from the walls. Under this model, there is no stress distribution (Supplementary Fig S9C). The continued pressing against the wall does occur when modeled as a contractile shell and passive core. When modeled in this way, without the walls of the well, we see this results in an outward “bowing” at the flat ends (Supplementary Fig S9D). In the oblong tissue model when the well wall is included, the contractile regions were primarily in tension. At the round caps, the third principal stress falls to near zero. The wall contacting regions were experiencing compression at similar levels to the intermediate and core regions (Figure 7J, K).

The results of our models suggest that geometry combined with the contractile shell drives regions of surface compression, which correlate to reduced hepatocytic differentiation and reduced ECAD expression. To explore this relationship further, we fabricated “double pillar” and “dumbbell” shaped microtissues (Supplementary Fig S10). While similar to the oblong design, the model predicted the presence of the pillars cause the tissues to contract away from the walls, eliminating any compressed surfaces (Fig 8A, Supplementary Fig S10C,D). This behavior was confirmed experimentally (Fig 8B). Here we observed that the entire periphery contained increased HNF4a positive cells and increased ECAD expression, including the flat sides (Fig 8C,D). We also observed the cortical actin ring around the periphery (Supplementary Fig S10E). The model predicts that the dumbbell microtissues contract such that only the center “bridge region” is compressed against the well wall (Fig 8E, Supplementary Fig S10F, G), which was confirmed experimentally (Fig 8F). Here increased HNF4a positive cells and ECAD expression was found around the periphery, except near this flat bridge region (Fig 8G,H). The

cortical actin was also found at the periphery, with some decrease at these flat sections (Supplementary Fig S10H).

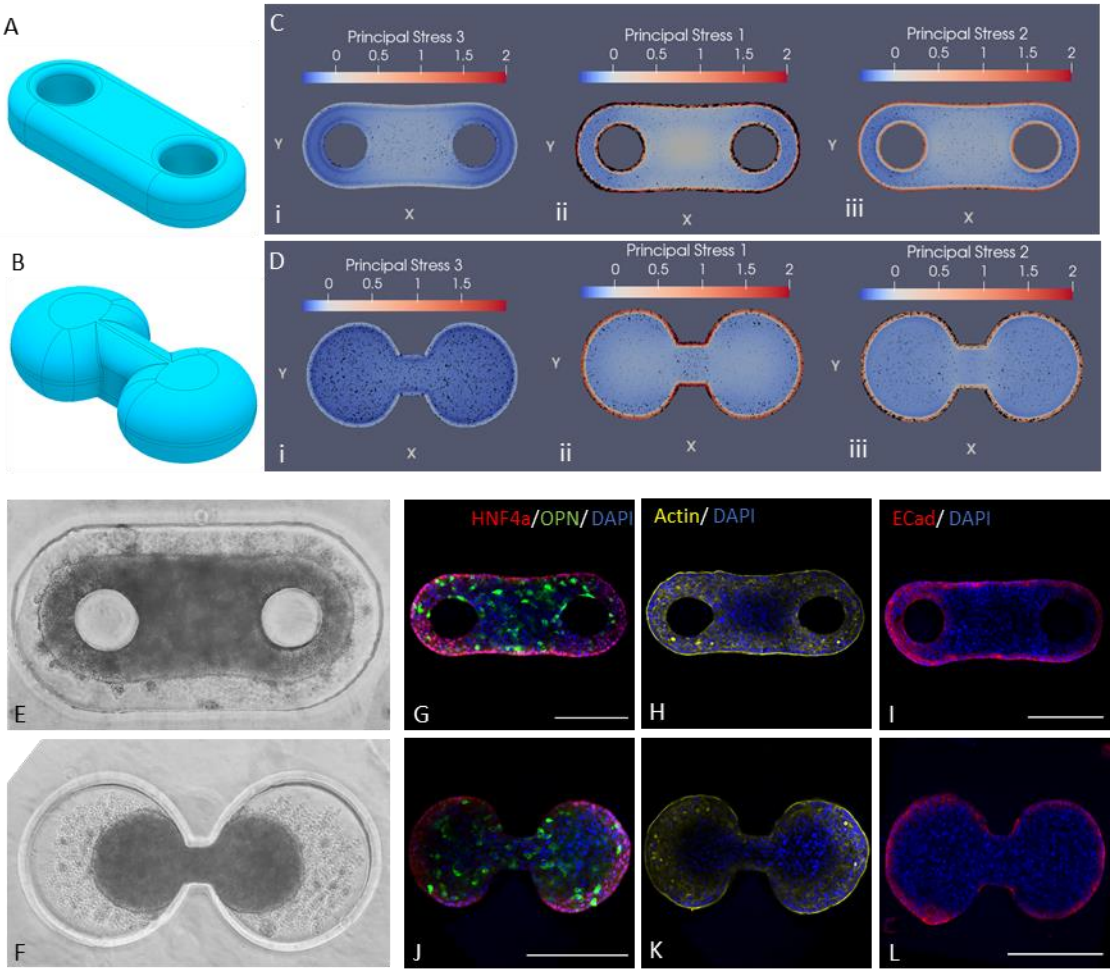

Figure 8. Behavior of double pillar and dumbbell microtissues. CAD model used for FEM simulation of the double pillar (A) and dog bone (B) tissues. Simulated principal stresses for the center XY slice of a (C) double pillar and (D) dumbbell geometries. Stresses are given in relative units. Bright ield image of a (E) double pillar and (F) dumbbell microtissue. Confocal images the central slice of a representative (G-H) double pillar and (J-K) dumbbell microtissue stained for HNF4a (red), OPN (green), actin (yellow) and with DAPI (blue). Scale bar 200 µm. Confocal images the central slice of a representative (I) double pillar and (L) dumbbell microtissue stained for Ecad (red) and with DAPI (blue). Scale bar 200 µm.

Discussion

Method provides reproducible arrays of geometrically defined microtissues

The molded microwell-based microtissue fabrication method we implemented, when combined with the described imaging, analysis, and mechanical modeling pipelines, provided an effective platform for characterizing spatial patterns of differentiation in 3D as they related to geometry. The use of photolithography, etching, and soft lithography techniques produced consistent replicate microtissues with a variety of well-defined, high aspect ratio geometries. This included toroid geometries with 150 um inner diameter, which is comparable to the diameter of an embryonic mouse portal vein [51], providing for physiological relevance. It also enabled fabrication of cylinders, oblong shapes, dumbbells, and multi-pillar structures, which allowed us to impart varied compressive and tensile stress profiles.

Using the two step PDMS molding process outside of the cleanroom, we achieve a multilayer mold. The multilayer mold enables creation of a loading well, without the use of multiple lithography, mask alignment, and etching steps, or use of a 3D printer which while more versatile can be limited by resolution. This loading well permits smaller volumes for cell seeding and for immunostaining steps. The use of 4-Arm-PEG-Arcylate as the hydrogel base provides a suitably, non-fouling material with limited swelling to allow resolving small features. It is also readily modified with conjugation of biomolecules via Michael type addition, or inclusion of acylated molecules during polymerization, to make the wells adhesive or otherwise reactive, if desired for future applications. Though not considered in this study, the stiffness of the hydrogel can be modulated by varying molecular weight and monomer density of the PEG solution. This is relevant in the toroid and oblong wells, where the microtissue exerts force against the well and may experience an effect of the substrate stiffness.

Due to the modularity of the design and ease of implementation, these methods can be easily adapted to other 3D cell culture applications. Use of embryonic stem cells, induced pluripotent stem cells, or other primary progenitor cells in this system, possibly with an encapsulating matrix such as Matrigel, could be used to produce standardized embryoid bodies or organoids. Controlling 3D geometry could prove a powerful tool in guiding morphogenesis. The platform could also be used to generate standardized 3D tumor models of controlled geometry and characterize or screen for any impact of geometry on drug efficacy.

3D Liver progenitor cell microtissues form contractile shells with increased hepatocytic differentiation

In the 3D liver progenitor cell microtissues, we observed a distinct spatial pattern of cells differentiating towards hepatocytic fate at the outer shell of cylinder tissues, with significantly reduced hepatocytic cells through the core. This was accompanied by an increase in e-cadherin expression, and a layer of increased actin expression. This pattern was consistent with a model of mechanical polarization at the boundary causing an effective tissue surface tension [52, 53]. Under this model, the outer shell develops a higher degree of contractility owing to the cortical actin layer, causing the cells to have high tension resolved across cell-cell interfaces [54]. Development of a tissue surface tension is especially expected in embryonic tissues, possibly due to osmolarity differences between interstitial fluid and cell culture media [42]. Recent work by Lee et al., directly measured this phenomena in similarly formed tissues [46]. These results suggest that cell-cell tension correlates with hepatocytic differentiation. This is supported by our observation that hepatocytic cell patterning at the outer surface was reduced by treatment with blebbistatin. This is consistent with our previously reported observations in 2D constrained islands, where the central region showed the highest hepatocytic differentiation [29], where the highest cell-cell tension is generated [55-57].

Compression reduces hepatocytic differentiation

In the toroid microtissues, we observed high hepatocytic differentiation at the tissue-media interface region of the outer shell and low hepatocytic differentiation throughout the core. Hepatocytic differentiation was low at the region contracted against the center PEG pillar. Since the PEG hydrogel used is non-adhesive and non-fouling, biochemically this interface would be expected to behave like the tissue-media interface. Thus, we would expect to observe similar mechanical polarization and high hepatocytic differentiation. The difference between these regions demonstrates an impact geometry and mechanical loading. ECAD expression followed the same pattern as hepatocytic differentiation. We also observed a cortical actin shell in these tissues, was somewhat reduced at the pillar contacting region.

Using microgel force sensors, we observed that the interiors of both tissue types were in compression. This supports the model of a contractile shell. It also suggested that regions in compression tended to be low in hepatocyte differentiation. We developed a finite element model in attempt to further understand this behavior. We had initially chosen the toroid geometry to mimic the portal vein region, and the prediction from previous models that a contracting toroid around a pillar yields nonuniform stress [20]. Based on the patterning of phenotype, e-cadherin, and actin, and the microgel results, we modeled the tissues with a contractile shell and passive core as described previously [46]. Under these assumptions, the outer shell is experiencing tension across what would be cell-cell interfaces, and the core is entirely in near uniform compression. In the toroid model, the entire shell is in cell-cell tension, and the core is in near uniform compression. However, at the pillar contacting boundary, the tissue experiences a significant compressive stress normal to the boundary. This suggests that compression, whether experienced across the core or against the well feature, decreases the likelihood of hepatocytic differentiation. Treatment with blebbistatin allows hepatocytic

differentiation to permeate further into the microtissue structure, possibly due to reduced cell force derived compression, supporting this hypothesis.

Our observations of progenitor differentiation within the oblong microtissues provide further support for the model assumptions and relation to phenotype. The oblong microtissues, once aggregated, continue to contact the walls at the flat region throughout culture. This final geometry would be predicted during condensation under a tissue surface tension model, as the tissues approach an energetically favorable spherical configuration, constrained by the well. However, if contraction occurs following condensation, uniform contraction would cause the tissues to contract away from the walls, which has been observed in tissues of other cell types [11]. The behavior of being “pressed” against the flat walls only occurs given a contractile shell and passive core, which predicts that compressive stresses occur at the flat sides, normal to the boundary. These compressed regions correlate to the regions of reduced hepatocytic differentiation and e-cadherin expression at the boundary. In the double pillar tissues, where the condensation leads to contraction away from the peripheral walls, there is no predicted compression and no region of excluded HNF4a expression. Though the mechanism relating compression to reduced hepatocytic differentiation remains unknown, recent work has demonstrated that compression can alter transcriptional behavior and cause depolymerization of actin [58]. Here the tensile contractile shell and the resolved compressive regions follow from mechanical polarization at the boundary. This is often associated with tissue-media boundaries in 3D culture, however mechanical polarization at tissue-tissue boundaries has been observed in vivo, causing local increases in cortical tension and taking part in cell sorting [59]. While in this system the PEG boundaries provide a non-adhesive service unlike what would be encountered in vivo, compressive forces can be achieved within adhesive matrices in some geometries, and thus may arise in vivo [50].

It is also important to note that in this system lack of curvature is closely tied to compressive regions. There is growing literature that cells and tissues respond to surface curvature in the microenvironment [60-63] . The flat compressive regions in oblong microtissues have zero curvature, while the pillar contacting region has non-zero median curvature but zero Gaussian curvature [64]. There is evidence that cells respond differently to these curvature types [65]. The double pillar microtissue results suggest that flat regions are still pushed towards hepatocytic fate in the absence of compression. However, when free from the it may be possible for sufficient curvature can form. Additionally, in 2D monolayers, hepatocytic differentiation occurs despite the flat plane geometry. However, it is possible that the response to curvature or relationship between curvature, stress, and phenotype are sensitive to other variables such as the adhesion molecule (i.e. integrin vs. cadherin) or stiffness.

Compression, EGF increase biliary differentiation

The ability to produce consistent, replicate 3D microtissues and spatially analyze single cell behavior enable characterizing the more subtle effect of geometry on biliary differentiation. Biliary differentiation, as identified by OPN expression was found throughout the inner region of the structures, regions expected to be under compression. Overall, toroid microtissues had a higher level of biliary differentiation. Our FEM model predicts that the compression across the core regions is higher in toroid compared to cylinder geometries, possibly explaining this difference. In both geometries, we observed increased biliary differentiation in the intermediate region just inside the outer shell. In the toroid tissues, biliary differentiation also increased near the surface contracting against the pillar. Within the 3D microtissues, these regions are predicted to be under the most compressive stress. Treatment with blebbistatin, which reduces compression induced by cell forces, reduces biliary differentiation, supporting the link between biliary phenotype and compression. We directly measured compression within the tissues using

alginate microgels. The imaged microgels throughout the interior of the tissues expanded upon tissue lysing, indicating they had been compressed by cell forces. This measurement technique does have several limitations. We did not track the relative vertical position of the microgel in the tissue, which the immunostaining data indicates is important. Further, the positions of the analyzed microgels are random, and based on bot uptake and ability to be imaged, the latter which is likely biased towards the bottom of the tissue where less penetration is required for imaging. Future work using a more optimized implementation of this or other emerging techniques to measure cell generated forces in 3D aggregates [5, 46, 66, 67] may provide a more quantified, precise stress map of the tissue to validate or refine our mechanical model. Nevertheless, the elastic round microgels reveal that the cylinder and toroid microtissues exert an average compressive stress of 200 to 1000 Pa, which is on the same order of magnitude as the shear storage modulus of the normal rat liver tissues [68], suggesting that our microtissues could mimic at least partial behavior of the living tissues.

Previous experiments utilizing 2D circular islands demonstrated a link between increased cell-substrate traction force and increased biliary differentiation. Here, blebbistatin treatment decreased overall biliary differentiation and eliminated the pattern [29]. Recent work has shown that cell to substrate tensile forces can impose vertical compressive forces on the nucleus, which can alter chromatin condensation, transcription factor activity, and gene expression, providing a possible link between our 2D and 3D observations [58, 69-71]. Studies using embryonic stem cells progenitors found that compressive stress can induce upregulation of SOX9, a transcription factor associated with biliary differentiation [72]. In bone remodeling and homeostasis, OPN is upregulated in response to compressive loading and is key to transduction of mechanical signals [73-76]. Though outside of a liver context, these findings support the mechanically sensitive nature of some biliary differentiation pathways. These data

demonstrate that compression may be an additional tool to control or pattern differentiation and morphogenesis in liver development as well as other stem cell and regenerative systems. This can be implemented in through physical compression or osmotic stress [72, 77].

Treatment with EGF increased biliary differentiation in all microtissue geometries, as well as amplified the spatial patterning aiding in characterizing these patterns. EGF has been previously demonstrated to play a role in both hepatocyte and biliary epithelium formation [78]. Our results add to growing evidence that EGF plays a role in biliary fate specification [79]. EGF has been used in various progenitor and human pluripotent stem cell lines to generate cholangiocytes in vitro [80-82]. More specifically, studies have reported EGF and EGFR induction of Notch signaling in the context of fate specification and morphogenesis [83, 84]. Further, Notch signaling is known to be mechanically sensitive [85, 86], thus there may be synergies between EGFR/Notch signaling with mechanical stress in 3D. This is one example of mechanisms which can be explored in this system. Modulation of other pathways through drug treatment, siRNA, or genetic editing, would permit exploring their relationships to force and geometry. Reliance on immunohistochemical staining can partially limit the refinement of differentiation kinetics. In future efforts, the integration of relevant fluorescent reporters with this platform would enable live cell imaging to track differentiation patterning over time and other dynamic processes.

Conclusion

We have implemented a microwell-based method to fabricate and analyze the behavior of geometrically-defined 3D liver progenitor microtissues. We modeled the mechanical behavior with a finite element method model. We observed in this system that cell derived forces create regions of varied compressive and tensile stress based on the multicellular geometry, which further drove spatial patterns of differentiation. These findings provide insight into how

geometric features may have a role in orchestrating biliary morphogenesis and overall liver development through mechanical signaling. Understanding these mechanisms could be leveraged in addressing developmental disorders and liver cancers, or in developing approaches to manufacture artificial livers from stem cells. Further, this integrated fabrication and analysis platform provides a framework to investigate the interactions between differentiation and mechanical loading in other stem and progenitor cell systems.

Disclosures

The authors indicate no potential conflicts of interest.

Acknowledgements

This work was supported by the National Science Foundation #1636175 to GU and by NIH GM 072744 to NW. Research reported in this publication was supported by the National Institute of Biomedical Imaging and Bioengineering of the National Institutes of Health under Award Number T32EB019944. The content is solely the responsibility of the authors and does not necessarily represent the official views of the National Institutes of Health. We gratefully acknowledge Hélène Strick-Marchand and Mary C. Weiss (Institut Pasteur) for the bipotential mouse embryonic liver (BMEL) cells. We acknowledge the Imaging Technology Group at the Beckman Institute for Advanced Science and Technology for help and advice with confocal microscopy.

CRediT authorship contribution statement

Ian C. Berg: Conceptualization, Methodology, Software, Validation, Formal analysis, Investigation, Data Curation, Writing - Original Draft, Writing - Review & Editing, Visualization, Project administration

Erfan Mohagheghian: Methodology, Software, Resources

Krista Habing: Investigation

Ning Wang: Methodology, Resources, Writing - Review & Editing, Supervision, Funding acquisition

Gregory H. Underhill: Conceptualization, Methodology, Validation, Resources, Writing - Review & Editing, Supervision, Funding acquisition

Data availability

Data available on request from the authors.

References

1. Vining, K.H. and D.J. Mooney, *Mechanical forces direct stem cell behaviour in development and regeneration.* Nature Reviews Molecular Cell Biology, 2017. **18**(12): p. 728-742.
2. Ladoux, B. and R.-M. Mège, *Mechanobiology of collective cell behaviours.* Nature Reviews Molecular Cell Biology, 2017. **18**(12): p. 743-757.
3. Lardennois, A., et al., *An actin-based viscoplastic lock ensures progressive body-axis elongation.* Nature, 2019. **573**(7773): p. 266-270.
4. Zhou, J., et al., *Force production and mechanical accommodation during convergent extension.* Development, 2015. **142**(4): p. 692.
5. Mohagheghian, E., et al., *Quantifying compressive forces between living cell layers and within tissues using elastic round microgels.* Nature Communications, 2018. **9**(1): p. 1878.
6. Passier, R., V. Orlova, and C. Mummery, *Complex Tissue and Disease Modeling using hiPSCs.* Cell Stem Cell, 2016. **18**(3): p. 309-321.
7. Shamir, E.R. and A.J. Ewald, *Three-dimensional organotypic culture: experimental models of mammalian biology and disease.* Nature Reviews Molecular Cell Biology, 2014. **15**(10): p. 647-664.
8. Eyckmans, J. and C.S. Chen, *3D culture models of tissues under tension.* Journal of Cell Science, 2017. **130**(1): p. 63.
9. Hwang, Y.-S., et al., *Microwell-mediated control of embryoid body size regulates embryonic stem cell fate via differential expression of WNT5a and WNT11.* Proceedings of the National Academy of Sciences, 2009. **106**(40): p. 16978.
10. Moeller, H.-C., et al., *A microwell array system for stem cell culture.* Biomaterials, 2008. **29**(6): p. 752-763.
11. Napolitano, A.P., et al., *Scaffold-free three-dimensional cell culture utilizing micromolded nonadhesive hydrogels.* BioTechniques, 2007. **43**(4): p. 494-500.
12. Nelson, C.M., J.L. Inman, and M.J. Bissell, *Three-dimensional lithographically defined organotypic tissue arrays for quantitative analysis of morphogenesis and neoplastic progression.* Nat Protoc, 2008. **3**(4): p. 674-8.
13. Mohr, J.C., J.J. de Pablo, and S.P. Palecek, *3-D microwell culture of human embryonic stem cells.* Biomaterials, 2006. **27**(36): p. 6032-6042.

14. Hsiao, C. and S.P. Palecek, *Microwell Regulation of Pluripotent Stem Cell Self-Renewal and Differentiation.* BioNanoScience, 2012. **2**(4): p. 266-276.
15. Azarin, S.M., et al., *Modulation of Wnt/β-catenin signaling in human embryonic stem cells using a 3-D microwell array.* Biomaterials, 2012. **33**(7): p. 2041-2049.
16. Gjorevski, N. and C.M. Nelson, *Endogenous patterns of mechanical stress are required for branching morphogenesis.* Integrative biology : quantitative biosciences from nano to macro, 2010. **2**(9): p. 424-434.
17. Radisky, D.C. and C.M. Nelson, *Regulation of mechanical stress by mammary epithelial tissue structure controls breast cancer cell invasion.* Oncotarget, 2013. **4**(4): p. 498-499.
18. Legant, W.R., C.S. Chen, and V. Vogel, *Force-induced fibronectin assembly and matrix remodeling in a 3D microtissue model of tissue morphogenesis.* Integrative Biology, 2012. **4**(10): p. 1164-1174.
19. Legant, W.R., et al., *Microfabricated tissue gauges to measure and manipulate forces from 3D microtissues.* Proceedings of the National Academy of Sciences, 2009. **106**(25): p. 10097.
20. Schell, J.Y., et al., *Harnessing cellular-derived forces in self-assembled microtissues to control the synthesis and alignment of ECM.* Biomaterials, 2016. **77**: p. 120-129.
21. Micsenyi, A., et al., *β-Catenin is temporally regulated during normal liver development.* Gastroenterology, 2004. **126**(4): p. 1134-1146.
22. Berg, T., et al., *Fibroblast growth factor 10 is critical for liver growth during embryogenesis and controls hepatoblast survival via β-catenin activation.* Hepatology, 2007. **46**(4): p. 1187-1197.
23. Schmidt, C., et al., *Scatter factor/hepatocyte growth factor is essential for liver development.* Nature, 1995. **373**(6516): p. 699-702.
24. Kodama, Y., et al., *The role of notch signaling in the development of intrahepatic bile ducts.* Gastroenterology, 2004. **127**(6): p. 1775-1786.
25. Clotman, F., et al., *Control of liver cell fate decision by a gradient of TGF beta signaling modulated by Onecut transcription factors.* Genes & development, 2005. **19**(16): p. 1849-1854.
26. Zong, Y., et al., *Notch signaling controls liver development by regulating biliary differentiation.* Development, 2009. **136**(10): p. 1727.
27. Kaylan, K.B., et al., *Combinatorial microenvironmental regulation of liver progenitor differentiation by Notch ligands, TGFβ and extracellular matrix.* Scientific Reports, 2016. **6**(1): p. 23490.
28. Kourouklis, A.P., K.B. Kaylan, and G.H. Underhill, *Substrate stiffness and matrix composition coordinately control the differentiation of liver progenitor cells.* Biomaterials, 2016. **99**: p. 82-94.
29. Kaylan, K.B., et al., *Spatial patterning of liver progenitor cell differentiation mediated by cellular contractility and Notch signaling.* eLife, 2018. **7**: p. e38536.
30. Lee, J., et al., *Influence of Biophysical Parameters on Maintaining the Mesenchymal Stem Cell Phenotype.* ACS Biomaterials Science & Engineering, 2015. **1**(4): p. 218-226.
31. Ma, Z., et al., *Self-organizing human cardiac microchambers mediated by geometric confinement.* Nature Communications, 2015. **6**(1): p. 7413.
32. Smith, Q., et al., *Cytoskeletal tension regulates mesodermal spatial organization and subsequent vascular fate.* Proceedings of the National Academy of Sciences, 2018. **115**(32): p. 8167.

33. Warmflash, A., et al., *A method to recapitulate early embryonic spatial patterning in human embryonic stem cells.* Nature Methods, 2014. **11**(8): p. 847-854.
34. Nelson, C.M., et al., *Emergent patterns of growth controlled by multicellular form and mechanics.* Proceedings of the National Academy of Sciences of the United States of America, 2005. **102**(33): p. 11594.
35. Gomez, E.W., et al., *Tissue geometry patterns epithelial–mesenchymal transition via intercellular mechanotransduction.* Journal of Cellular Biochemistry, 2010. **110**(1): p. 44-51.
36. Muncie, J.M., et al., *Mechanics regulate human embryonic stem cell self-organization to specify mesoderm.* bioRxiv, 2020: p. 2020.02.10.943076.
37. Silver, B.B., et al., *Epithelial tissue geometry directs emergence of bioelectric field and pattern of proliferation.* Molecular Biology of the Cell, 2020: p. mbc.E19-12-0719.
38. Qin, D., Y. Xia, and G.M. Whitesides, *Soft lithography for micro- and nanoscale patterning.* Nat Protoc, 2010. **5**(3): p. 491-502.
39. Yang, M.T., N.J. Sniadecki, and C.S. Chen, *Geometric Considerations of Micro- to Nanoscale Elastomeric Post Arrays to Study Cellular Traction Forces.* Advanced Materials, 2007. **19**(20): p. 3119-3123.
40. Wen, J.H., et al., *Interplay of matrix stiffness and protein tethering in stem cell differentiation.* Nature Materials, 2014. **13**(10): p. 979-987.
41. Strick-Marchand, H. and M.C. Weiss, *Inducible differentiation and morphogenesis of bipotential liver cell lines from wild-type mouse embryos.* Hepatology, 2002. **36**(4): p. 794-804.
42. Lou, X., et al., *A Rapid and Efficient 2D/3D Nuclear Segmentation Method for Analysis of Early Mouse Embryo and Stem Cell Image Data.* Stem Cell Reports, 2014. **2**(3): p. 382-397.
43. Goldberg, I.G., et al., *The Open Microscopy Environment (OME) Data Model and XML file: open tools for informatics and quantitative analysis in biological imaging.* Genome Biology, 2005. **6**(5): p. R47.
44. Geuzaine, C. and J.-F. Remacle, *Gmsh: A 3-D finite element mesh generator with built-in pre- and post-processing facilities.* International Journal for Numerical Methods in Engineering, 2009. **79**(11): p. 1309-1331.
45. Maas, S.A., et al., *FEBio: Finite Elements for Biomechanics.* Journal of Biomechanical Engineering, 2012. **134**(1).
46. Lee, W., et al., *Dispersible hydrogel force sensors reveal patterns of solid mechanical stress in multicellular spheroid cultures.* Nature Communications, 2019. **10**(1): p. 144.
47. Ahrens, J., B. Geveci, and C. Law, *36 - ParaView: An End-User Tool for Large-Data Visualization*, in *Visualization Handbook*, C.D. Hansen and C.R. Johnson, Editors. 2005, Butterworth-Heinemann: Burlington. p. 717-731.
48. Wickham, H., *ggplot2: Elegant Graphics for Data Analysis*. 1 ed. Use R! 2009: Springer-Verlag New York. VIII, 213.
49. Team, R.C., *R: A language and environment for statistical computing.* 2013. **3**(3).
50. Gjorevski, N. and Celeste M. Nelson, *Mapping of Mechanical Strains and Stresses around Quiescent Engineered Three-Dimensional Epithelial Tissues.* Biophysical Journal, 2012. **103**(1): p. 152-162.
51. Villeneuve, J., et al., *Immunohistochemical study of the phenotypic change of the mesenchymal cells during portal tract maturation in normal and fibrous (ductal plate malformation) fetal liver.* Comparative Hepatology, 2009. **8**(1): p. 5.

52. Amack, J.D. and M.L. Manning, *Knowing the boundaries: Extending the differential adhesion hypothesis in embryonic cell sorting*. 2012, American Association for the Advancement of Science. p. 212-215.
53. Manning, M.L., et al., *Coaction of intercellular adhesion and cortical tension specifies tissue surface tension.* Proceedings of the National Academy of Sciences, 2010. **107**(28): p. 12517.
54. Riccobelli, D. and G. Bevilacqua, *Surface tension controls the onset of gyrification in brain organoids.* Journal of the Mechanics and Physics of Solids, 2020. **134**: p. 103745.
55. Maruthamuthu, V., et al., *Cell-ECM traction force modulates endogenous tension at cell–cell contacts.* Proceedings of the National Academy of Sciences, 2011. **108**(12): p. 4708.
56. Edwards, C.M. and U.S. Schwarz, *Force Localization in Contracting Cell Layers.* Physical Review Letters, 2011. **107**(12): p. 128101.
57. Mertz, A.F., et al., *Cadherin-based intercellular adhesions organize epithelial cell–matrix traction forces.* Proceedings of the National Academy of Sciences, 2013. **110**(3): p. 842.
58. Damodaran, K., et al., *Compressive force induces reversible chromatin condensation and cell geometry–dependent transcriptional response.* Molecular Biology of the Cell, 2018. **29**(25): p. 3039-3051.
59. Monier, B., A. Pélissier-Monier, and B. Sanson, *Establishment and maintenance of compartmental boundaries: role of contractile actomyosin barriers.* Cellular and Molecular Life Sciences, 2011. **68**(11): p. 1897-1910.
60. Altay, G., et al., *Imaging the Cell Morphological Response to 3D Topography and Curvature in Engineered Intestinal Tissues.* Frontiers in Bioengineering and Biotechnology, 2020. **8**: p. 294-294.
61. Yu, S.M., et al., *Substrate curvature affects the shape, orientation, and polarization of renal epithelial cells.* Acta Biomaterialia, 2018. **77**: p. 311-321.
62. Bade, N.D., et al., *Curvature and Rho activation differentially control the alignment of cells and stress fibers.* Science Advances, 2017. **3**(9): p. e1700150-e1700150.
63. Pieuchot, L., et al., *Curvotaxis directs cell migration through cell-scale curvature landscapes.* Nature Communications, 2018. **9**(1): p. 1-13.
64. Assoian, R.K., et al., *Cellular sensing of micron-scale curvature: a frontier in understanding the microenvironment.* Open Biology, 2019. **9**(10): p. 190155-190155.
65. Bade, N.D., et al., *Gaussian Curvature Directs Stress Fiber Orientation and Cell Migration.* Biophysical Journal, 2018. **114**(6): p. 1467-1476.
66. Dolega, M.E., et al., *Cell-like pressure sensors reveal increase of mechanical stress towards the core of multicellular spheroids under compression.* Nature Communications, 2017. **8**(1): p. 14056.
67. Moraes, C., et al., *Supersoft lithography: candy-based fabrication of soft silicone microstructures.* Lab on a Chip, 2015. **15**(18): p. 3760-3765.
68. Perepelyuk, M., et al., *Normal and Fibrotic Rat Livers Demonstrate Shear Strain Softening and Compression Stiffening: A Model for Soft Tissue Mechanics.* PloS one, 2016. **11**(1): p. e0146588-e0146588.
69. Alisafaei, F., et al., *Regulation of nuclear architecture, mechanics, and nucleocytoplasmic shuttling of epigenetic factors by cell geometric constraints.* Proceedings of the National Academy of Sciences, 2019. **116**(27): p. 13200.
70. Irianto, J., et al., *Osmotic challenge drives rapid and reversible chromatin condensation in chondrocytes.* Biophysical Journal, 2013. **104**(4): p. 759-769.

71. Werner, M., et al., *Surface Curvature Differentially Regulates Stem Cell Migration and Differentiation via Altered Attachment Morphology and Nuclear Deformation.* Advanced Science, 2017. **4**(2): p. 1600347.
72. McKee, C., et al., *Compression Induced Chondrogenic Differentiation of Embryonic Stem Cells in Three-Dimensional Polydimethylsiloxane Scaffolds.* Tissue Engineering - Part A, 2017. **23**(9-10): p. 426-435.
73. Hashimoto, M., et al., *Upregulation of Osteopontin Expression in Rat Spinal Cord Microglia after Traumatic Injury.* Journal of Neurotrauma, 2003. **20**(3): p. 287-296.
74. Muneaki, I., et al., *Osteopontin is required for mechanical stress-dependent signals to bone marrow cells.* Journal of Endocrinology. **193**(2): p. 235-243.
75. Takano-Yamamoto, T., *Osteocyte function under compressive mechanical force.* Japanese Dental Science Review, 2014. **50**(2): p. 29-39.
76. Terai, K., et al., *Role of Osteopontin in Bone Remodeling Caused by Mechanical Stress.* Journal of Bone and Mineral Research, 1999. **14**(6): p. 839-849.
77. Montel, F., et al., *Stress Clamp Experiments on Multicellular Tumor Spheroids.* Physical Review Letters, 2011. **107**(18): p. 188102.
78. Michalopoulos, G.K., et al., *HGF-, EGF-, and dexamethasone-induced gene expression patterns during formation of tissue in hepatic organoid cultures.* Gene expression, 2003. **11**(2): p. 55-75.
79. Pellat, A., J. Vaquero, and L. Fouassier, *Role of ErbB/HER family of receptor tyrosine kinases in cholangiocyte biology.* Hepatology, 2018. **67**(2): p. 762-773.
80. Tanimizu, N., et al., *Long-term culture of hepatic progenitors derived from mouse Dlk⁺ hepatoblasts.* Journal of Cell Science, 2004. **117**(26): p. 6425.
81. Dianat, N., et al., *Generation of functional cholangiocyte-like cells from human pluripotent stem cells and HepaRG cells.* Hepatology, 2014. **60**(2): p. 700-714.
82. Ogawa, M., et al., *Directed differentiation of cholangiocytes from human pluripotent stem cells.* Nature Biotechnology, 2015. **33**(8): p. 853-861.
83. Kitade, M., et al., *Specific fate decisions in adult hepatic progenitor cells driven by MET and EGFR signaling.* Genes & development, 2013. **27**(15): p. 1706-1717.
84. Ningappa, M., et al., *The Role of ARF6 in Biliary Atresia.* PLOS ONE, 2015. **10**(9): p. e0138381.
85. Chowdhury, F., et al., *Defining Single Molecular Forces Required for Notch Activation Using Nano Yoyo.* Nano letters, 2016. **16**(6): p. 3892-3897.
86. Kovall, R.A., et al., *The Canonical Notch Signaling Pathway: Structural and Biochemical Insights into Shape, Sugar, and Force.* Developmental cell, 2017. **41**(3): p. 228-241.

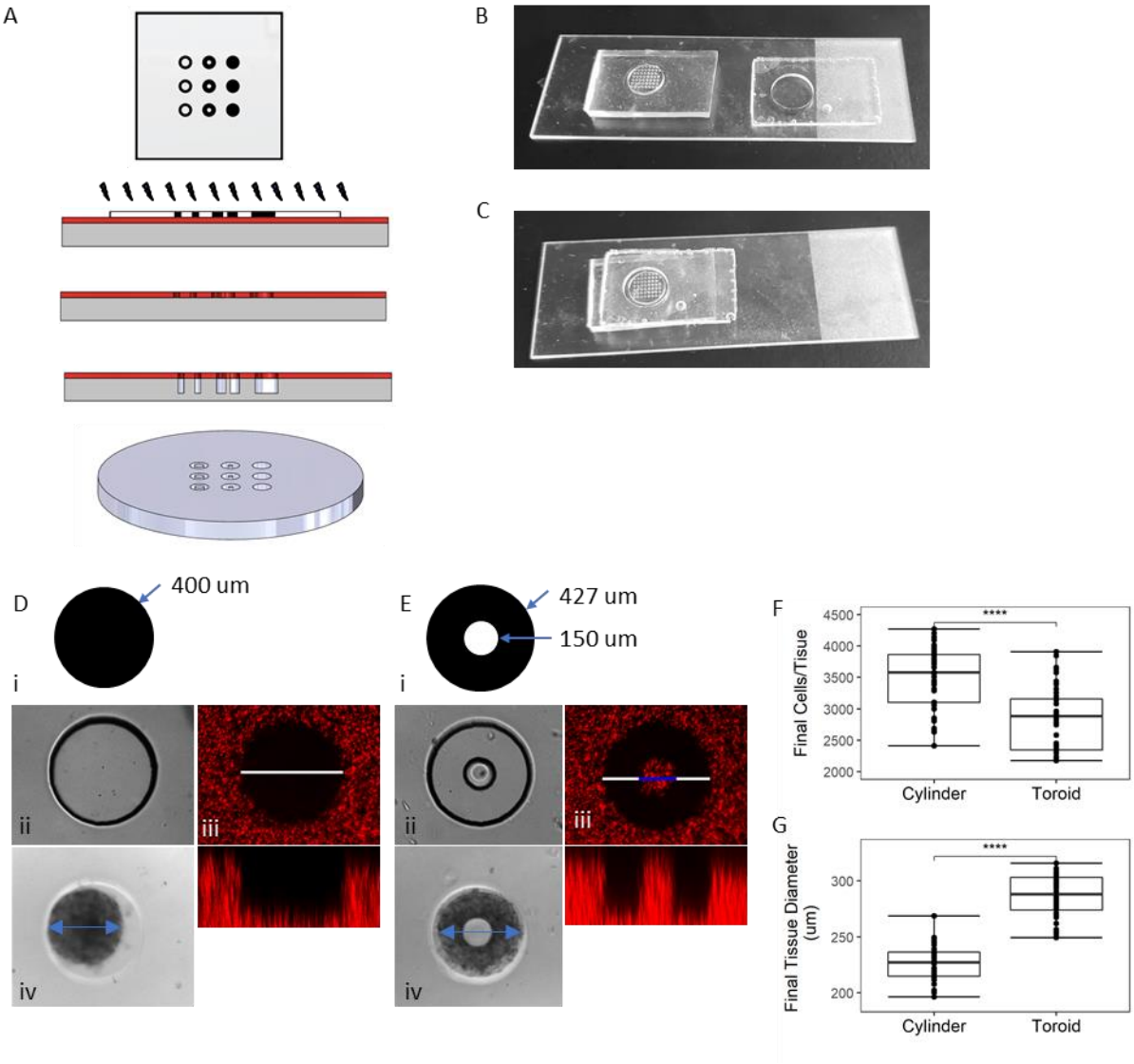

Supplementary Figure 1. Fabrication process and characterization of hydrogel substrates and microtissues. A) Schematic of master wafer preparation by photolithography and etching. B) Multilevel PDMS mold of one feature array. C) PDMS mold with 1 mm gasket. D) Characterization of cylinder well. i) Feature design used in mask. ii) Bright field image of cylinder well. iii) XY (top) and XZ (bottom) confocal images of cylinder well with fluorescent beads mixed in hydrogel. White bar indicates 400 µm. iv) Brightfield image of cylinder tissue. Blue line indicates tissue diameter. E) Characterization of toroid well. i) Feature design used in mask. ii) Brightfield image of toroid well. iii) XY (top) and XZ (bottom) confocal images of toroid well with fluorescent beads mixed in hydrogel. White and blue bars indicates 427 and 150 µm. iv) Brightfield image of toroid tissue. F) Number of cells counted from segmentation per tissue after 72 hours of culture. G) Final outer diameter of tissues after 72 hours of culture. **** $p <= 0.0001$.

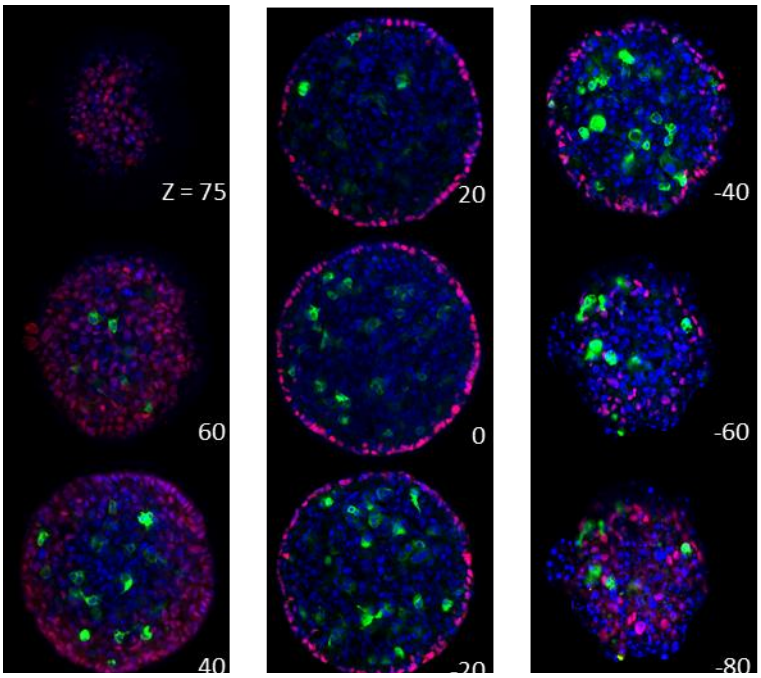

Supplementary Figure S2. HNF4a and OPN distribution across cylinder microtissue. XY confocal slices of a representative cylinder tissue stained for hepatocytic marker HNF4a (red), biliary marker OPN (green), and with DAPI (blue). Slices labeled by Z distance from the approximate center.

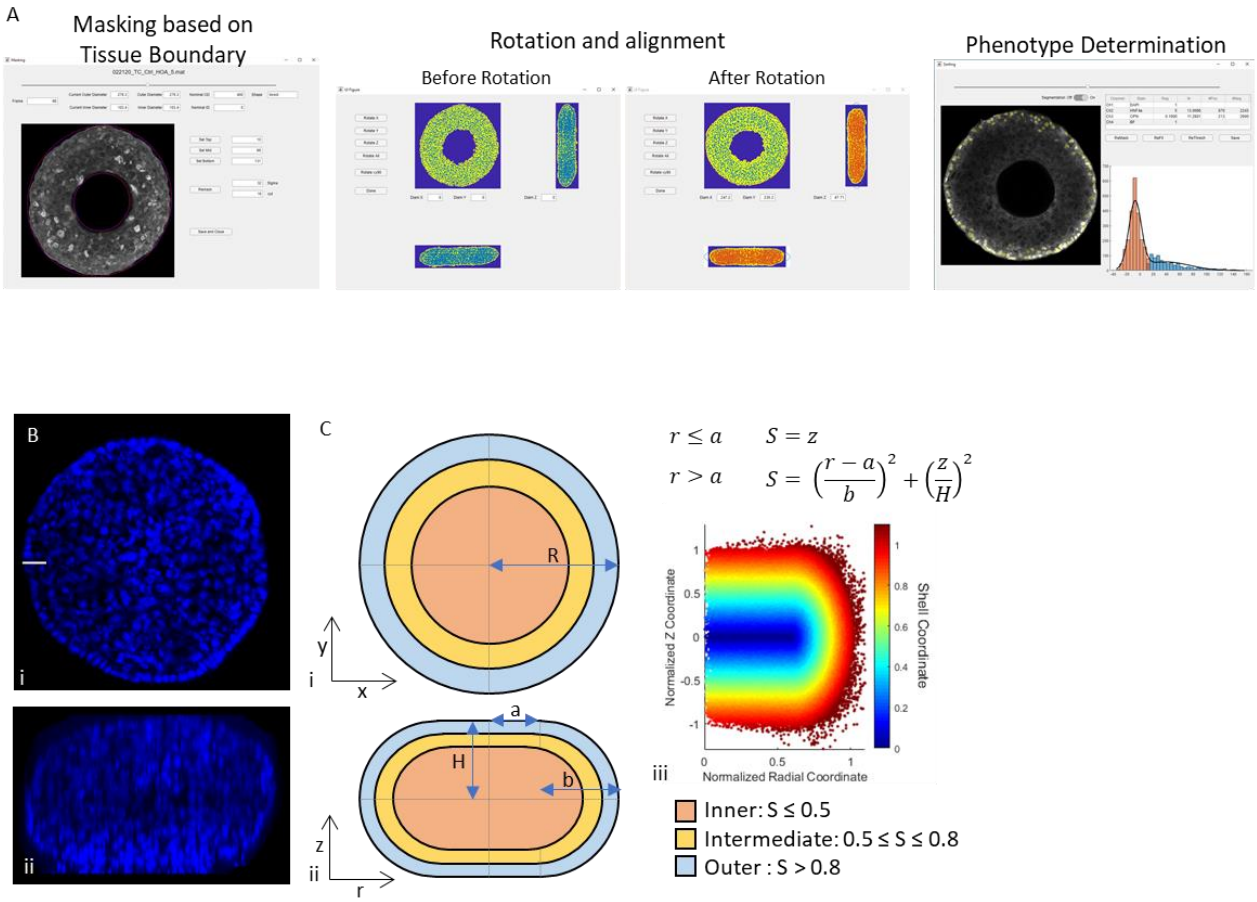

Supplementary Figure S3. Analysis of segmented data in 3D. A) Outline of process used to identify microtissue boundary, rotate locations in 3D for alignment and normalizing locations for comparison across microtissues, and identifying phenotype based on stain intensity. B) Representative central XY (i) and central XZ (ii) planes of a cylinder tissue stained for DAPI, imaged confocally. C) Approximated geometry of cylinder microtissues, divided into regions in the (i) XY and (ii) ZR planes. iii) Shell coordinate for nuclei plotted in the RZ plane.

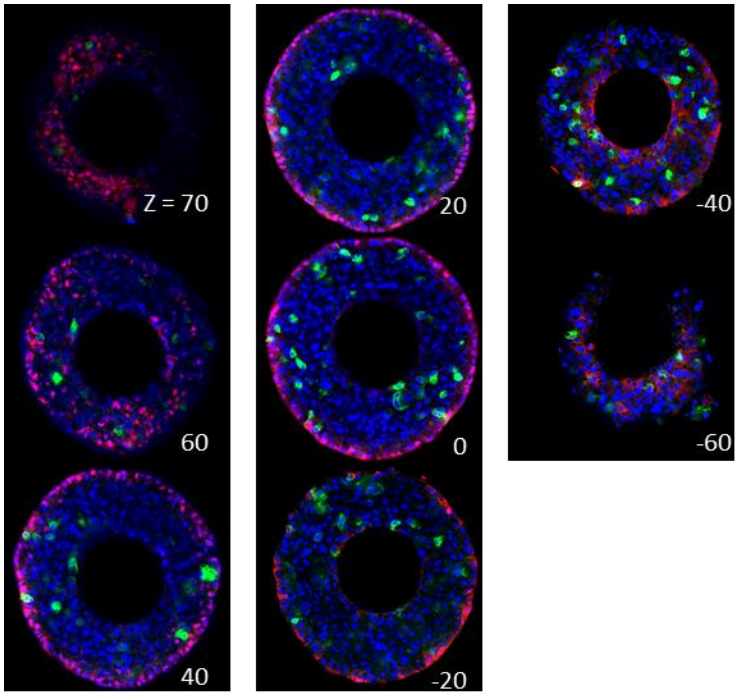

Supplementary Figure S4. HNF4a and OPN distribution across toroid microtissue. XY confocal slices of a representative toroid microtissue stained for hepatocytic marker HNF4a (red), biliary marker OPN (green), and with DAPI (blue). Slices labeled by Z distance from the approximate center.

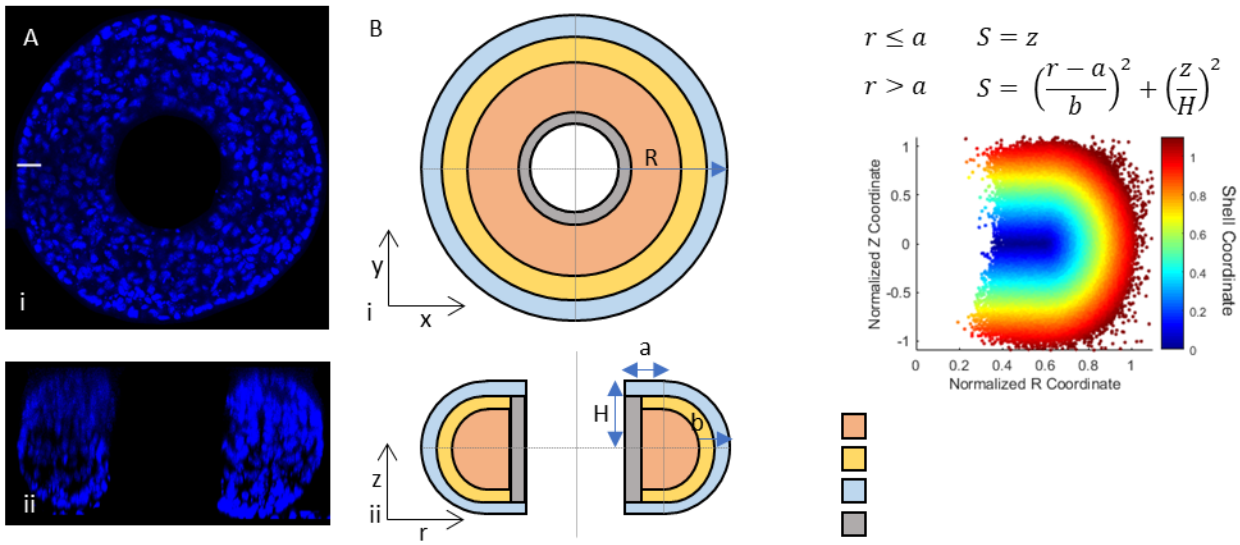

Supplementary Figure S5. Geometry of toroid microtissues. A) Representative central XY (i) and central XZ (ii) planes of a cylinder microtissue stained for DAPI, imaged confocally. B) Approximated geometry of cylinder microtissues, divided into regions in the (i) XY and (ii) ZR planes. iii) Shell coordinate for nuclei plotted in the RZ plane.

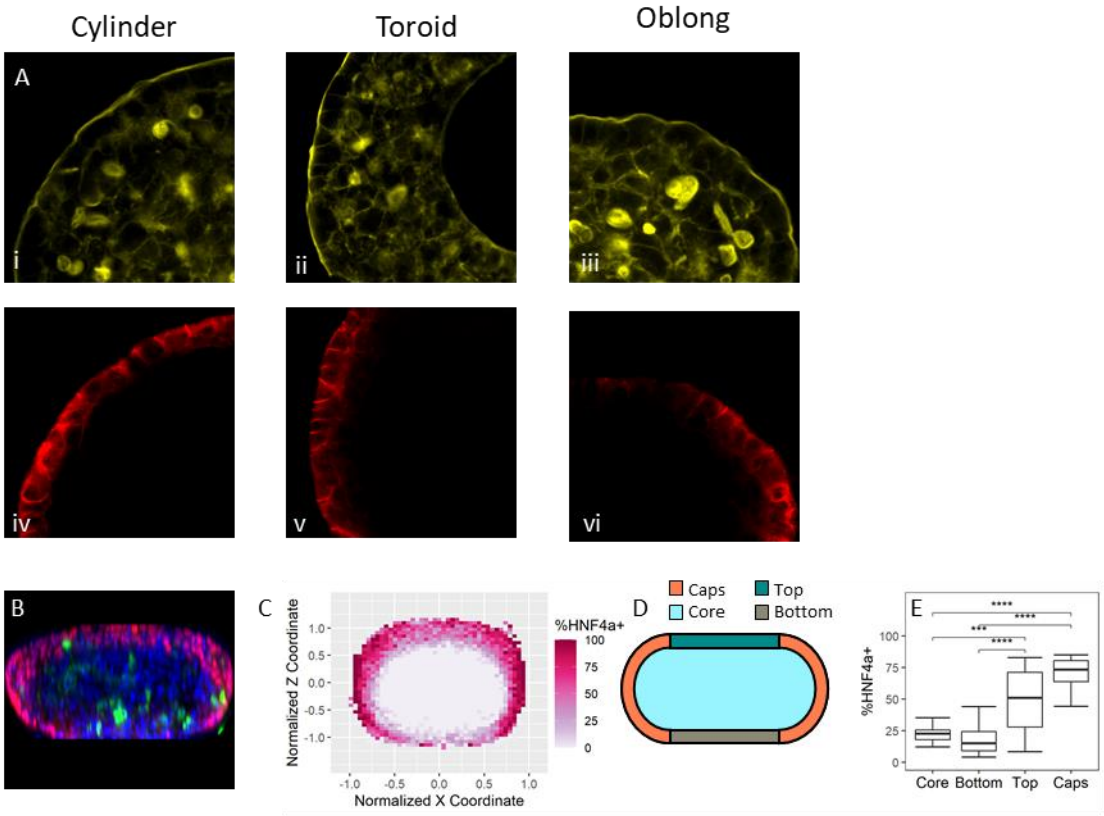

Supplementary Figure S6. Actin, E-Cadherin, and HN4a in 3D BMEL microtissues. A) Increased magnification view of actin staining in cylinder, toroid, and oblong microtissues. Increased magnification view of E-cadherin staining in cylinder, toroid, and oblong microtissues. B) Confocal XZ image slice of a representative 200 µm wide oblong geometry stained for HNF4a (red), OPN (green), and with DAPI (blue). Scale bar 100 µm. C) Percentage of HNF4a positive cells in XZ space in the center 25% of the microtissue thickness from N=## 200 µm wide toroids. D) Descriptive regions of oblong microtissues. E) Percentage of HNF4a positive cells in the core, flat, and regions of 200 µm geometries. ***p<=0.001, **** p <= 0.0001.

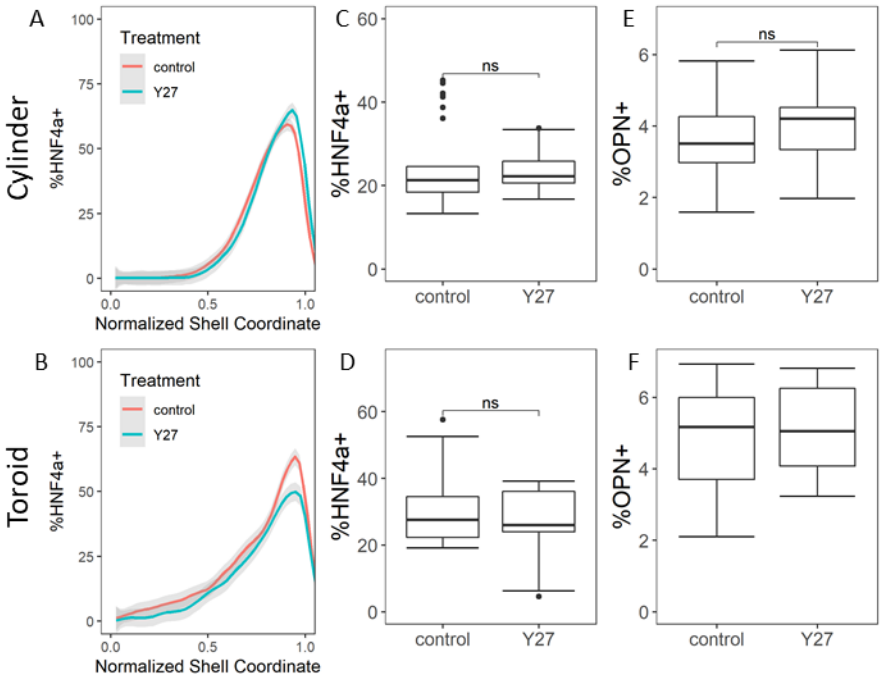

Supplementary Figure S7. Effects of Y-27632 Treatment. A,B) %HNF4a positive versus shell coordinate for untreated and Y27 treated cylinder and toroid microtissues. C-F) Overall %HNF4a and %OPN positive cells per microtissues in untreated and Y27-treated cylinders and toroids.

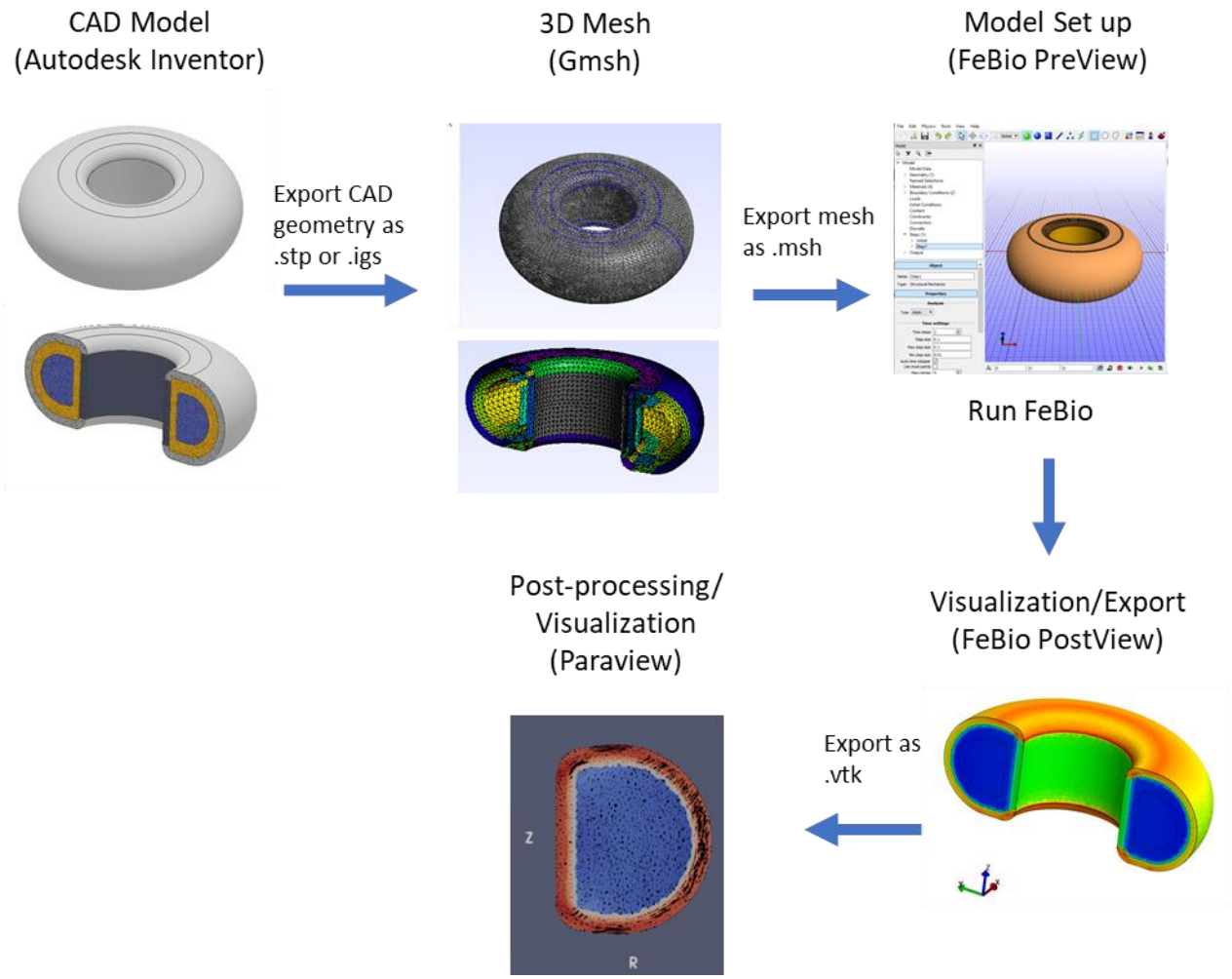

Supplementary Figure S8. FEM modeling with open source software. Outline of process and software used to create, run, and analyze FEM models. 3D Tissue geometries were drawn in Autodesk inventor. These geometries were exported as STEP or IGES files. The finite element mesh generator software Gmsh was used to generate mesh files for each geometry. The model was produced using the FEBio software suite. The PreView software was used to import the geometry, set boundary conditions, and specify material properties. The simulation was run using the FeBio solver. Simulation results were visualized in the PostView program, which was also used to export results as a VTK file. Paraview was used to calculate principle stresses, visualize data, and generate figures.

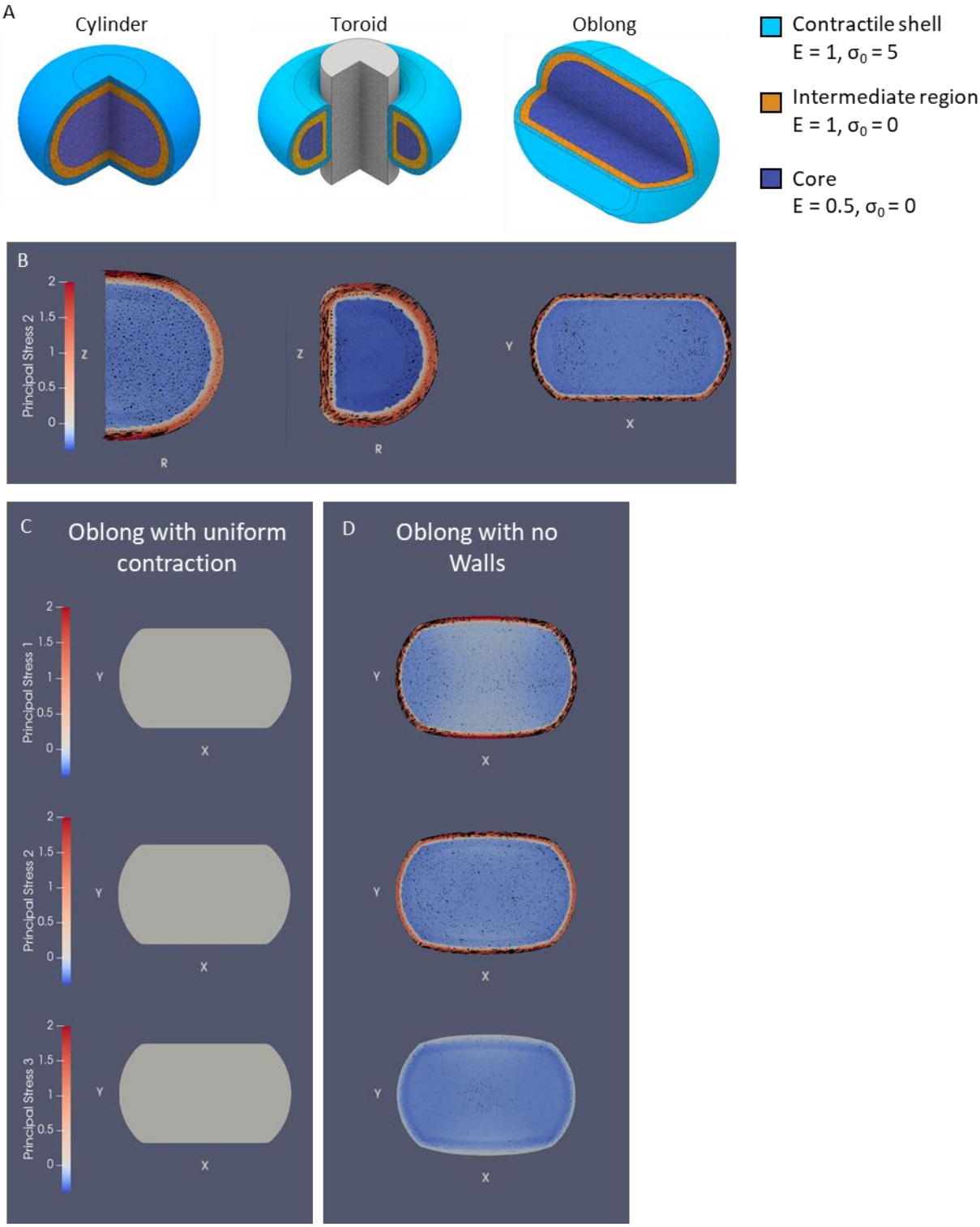

Supplementary Figure S9. FEM modeling of microtissue contraction. A) 3D models of the cylinder, toroid, and oblong geometries used in the FEM model. Cutaways show the contractile shell, intermediate, and core regions. B) Simulated second principal for an RZ slice of a cylinder and toroid microtissue, and the center XY slice of an oblong geometry. C) Simulated principal stresses for the central XY slice (oblong) with uniform contraction. D) Simulated principal stresses for the central XY slice (oblong) with a passive force, not constrained by walls. Stresses are given in relative units.